Validity assessment of SAMOSA retracking for fully-focused SAR altimeter waveforms

Ehlers, Frithjof; Schlembach, Florian; Kleinherenbrink, Marcel; Slobbe, Cornelis

Validity assessment of SAMOSA retracking for fully-focused SAR altimeter waveforms

Frithjof Ehlers [a,*], Florian Schlembach [b], Marcel Kleinherenbrink [a], Cornelis Slobbe [a]

[a] *Geoscience & Remote Sensing, Delft University of Technology (TU Delft), 2628 CN Delft, Netherlands*
[b] *Deutsches Geodätisches Forschungsinstitut, Technical University of Munich (DGFI-TUM), Munich, Germany*

Abstract

We demonstrate in this work how we can take advantage of known unfocused SAR (UF-SAR) retracking methods (e.g. the physical SAMOSA model) for retracking of fully-focused SAR (FF-SAR) waveforms. Our insights are an important step towards consistent observations of sea surface height, significant wave height and backscatter coefficient (wind speed) with both UF-SAR and FF-SAR. This is of particular interest for SAR altimetry in the coastal zone, since coastal clutter may be filtered out more efficiently in the high-resolution FF-SAR waveform data, which has the potential to improve data quality. We implemented a multi-mission FF-SAR altimetry processor for Sentinel-3 (S3) and Sentinel-6 Michael Freilich (S6), using a back-projection algorithm, and analysed ocean waveform statistics compared to multilooked UF-SAR. We find for Sentinel-3 that the averaged power waveforms of UF-SAR and FF-SAR over ocean are virtually identical, while for Sentinel-6 the FF-SAR power waveforms better resemble the UF-SAR zero-Doppler beam. We can explain and model the similarities and differences in the data via theoretical considerations of the waveform integrals. These findings suggest to use the existing UF-SAR SAMOSA model for retracking S3 FF-SAR waveforms but the SAMOSA zero-Doppler beam model for S6 FF-SAR waveforms, instead. Testing the outlined approach over short track segments, we obtain range biases between UF-SAR and FF-SAR lower than 2 mm and significant wave height biases lower than 5 cm.
© 2022 COSPAR. Published by Elsevier B.V. This is an open access article under the CC BY license (http://creativecommons.org/licenses/by/4.0/).

1. Introduction

Fully-focused synthetic aperture radar (FF-SAR Egido and Smith, 2017) processing is a novel processing strategy for SAR altimeter data and can be applied to CryoSat-2 (CS2), Sentinel-3 (S3) and Sentinel-6 Michael Freilich (S6). In contrast to unfocused SAR processing (UF-SAR, also known as delay-Doppler processing Raney, 1998) with an along-track resolution of approximately 300 m, fully-focused SAR pushes the theoretical along-track resolution

limit to approximately 0.5 m by coherent processing of pulse echoes over the whole target illumination time. This does not improve the resolution in across-track direction: as with UF-SAR processing, depending on the surface roughness, the footprint extends in this direction for several km. A particular difference between the missions is that full exploitation of FF-SAR for CS2 and S3 is hampered by the closed-burst operation mode (or lacunar sampling), as opposed to S6 open-burst operation mode (Egido and Smith, 2017; Donlon et al., 2021), see Fig. 1 for illustration. In the first case, the non-continuous sampling causes along-track grating lobes (target copies) to appear at along-track distances of ∼ 95 m. Despite the difference between the along- and across-track resolutions and the closed-burst

* Corresponding author.
 E-mail addresses: f.ehlers@tudelft.nl (F. Ehlers), florian.schlembach@tum.de (F. Schlembach), m.kleinherenbrink@tudelft.nl (M. Kleinherenbrink), d.c.slobbe@tudelft.nl (C. Slobbe).
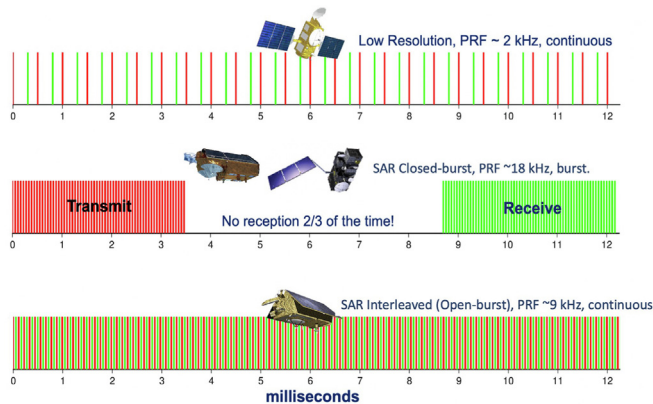
Fig. 1. Figure taken from Donlon et al. (2021): Evolution of satellite radar altimeter chronograms highlighting the optimal use of available pulse transmit and receive time when using the Sentinel-6 interleaved (**open-burst mode**) measurement approach (bottom) compared to Sentinel-3 and CryoSat-2 (**closed-burst mode**, center) and Jason series that provides LRM measurements only (top).

operations of CS2 and S3, FF-SAR processing can distinguish small targets in highly heterogeneous scenes. Therefore, it has high potential to increase altimeter data quality over inland water bodies and ice sheets (Kleinherenbrink et al., 2020a; McMillan et al., 2020; Aublanc et al., 2022; Nielsen et al., 2021), and to enhance the measurement capabilities of altimeters to swell monitoring (Rieu et al., 2021b; Altiparmaki et al., 2022). Meanwhile, a public FF-SAR processor for S3 has already been made available (Rieu et al., 2021a) and a dedicated algorithm has been described to lower computational costs (Guccione et al., 2018). On-demand-processing of CS2 data is offered via the P-PRO Altimetry services on earthconsole.eu. Therefore, FF-SAR processed data are becoming widely accessible.

One of the interests in FF-SAR for ocean applications is the coastal zone: On the one hand, it has been demonstrated that the vertical motion of the sea surface due to waves limits the achievable effective along-track resolution over such surfaces to several tens of meters (Fig. A.5 Buchhaupt et al., 2021) and that grating lobes from closed-burst sampling (in case of CS2 and S3, but not S6) effectively prevent to measure Sea Surface Height on scales below 200 m (Moreau et al., 2022). On the other hand, each fully-focused along-track sample is still a statistically independent speckle noise realisation (Egido and Smith, 2017) and the superimposed and highly problematic coastal clutter (e.g. discussed in Vignudelli et al., 2011; Passaro et al., 2018; Schlembach et al., 2022) is nonetheless resolved with several meters. Hence, less waveforms are affected by this clutter in FF-SAR, and therefore, more useful ocean samples are available for retracking, with potential benefits for altimetry data quality. However, no dedicated analytical ocean surface return model has been developed yet to accurately estimate the ocean parameters (sea surface height, significant wave height, and backscatter coefficient) from FF-SAR. For UF-SAR, such a model is provided by

SAMOSA (Ray et al., 2015; Dinardo, 2020). Therefore, we here focus on proper retracking techniques for FF-SAR over ocean, before coastal applications can be addressed in future work. It was argued that the zero-Doppler beam of the SAMOSA model should provide a good fit to CS2 FF-SAR ocean waveforms (Egido and Smith, 2017), based on the great similarity of the flat surface responses. This analysis omitted the influence of the grating lobes and resulted in some second order differences of the retracked parameters, especially in range. Other works suggest that the S3 FF-SAR ocean waveforms are very similar to multilooked UF-SAR waveforms (Rieu et al., 2018). Since the instrument on-board CS2 (SIRAL) and S3 (SRAL) operate almost identical SAR modes, these observations suggest i) that the SAMOSA zero-Doppler beam provides no good fit in general, and ii) that the FF-SAR waveform shape depends at least on changing processing parameters such as the coherent integration time. This influence has indeed been described implicitly (see section A.3. Buchhaupt et al., 2021). In the same work, an extensive analytic expression of the CS2 FF-SAR waveform in Fourier space is provided (see Eq. 66), which requires Discrete Fourier Transform in each iteration of the retracking (similar to Buchhaupt et al. (2018)). However, the study was purely theoretical and involved no real data. To our knowledge, no fully analytic description of the FF-SAR waveforms in the spirit of the SAMOSA model (in time-domain) has been provided and demonstrated.

The most rigorous way of approaching this problem would be to derive a SAMOSA-like model for FF-SAR from scratch. The question is, however, whether such an effort is required. Indeed, if it could be shown that FF-SAR and UF-SAR ocean power waveforms had similar shapes, then i) the same SAMOSA-based retracking algorithms would be applicable, ii) implementation efforts would be minimized and iii) the geophysical estimates would be consistent with UF-SAR. To our knowledge, such a comparison has never been systematically performed. In this work, we first compare averaged ocean waveforms from UF-SAR and FF-SAR processed data for both S3 and S6 for a few data cases and identical processing settings. We then use established theory from Brown (1977), Ray et al. (2015) in order to generalize our findings. Making this step requires deriving an improved description of the FF-SAR 2D impulse response function (2D IRF) compared to the existing approximations in Egido and Smith (2017, 2018), which will be discussed in depth.

The manuscript is organized as follows: Section 2 provides an overview of our approach, explains the data processing, introduces previous theoretical findings and lists the utilized data for this study. Section 3 starts with a comparison of average UF-SAR and FF-SAR ocean waveforms for S3 and S6. These results are then discussed by means of theoretical considerations in the remainder of the section. The limitations of our study are discussed in

Section 4, while the key findings are formulated in Section 5.

2. Methods and data

2.1. Overall approach

Our analysis comprises three components.

2.1.1. Comparison of averaged UF-SAR and FF-SAR ocean waveforms

The SAMOSA model approximates an ocean waveform without speckle noise. In reality, noise is present and may affect the UF-SAR and FF-SAR processed waveforms differently, which is why the ocean waveforms must be averaged before comparison. An along-track average over more than 100 km ground distance is applied to bring down speckle noise, after which the waveforms are normalized with their peak value. To obtain comparable FF-SAR and UF-SAR waveforms at the same posting rates, any influence due to deviating processing settings, calibrations, and input data must be ruled out. Hence, as in Egido et al. (2021b) the UF-SAR waveforms will be generated from a modified FF-SAR processor. See Sections Appendix 2.2 and 2.3 for further details about the processors. The UF-SAR and FF-SAR waveforms are both obtained at the FF-SAR posting rate corresponding to approximately 0.5–1 m ground resolution and with zero padding. Thus, S3 and S6 waveforms have 256 and 512 range gates, respectively. The waveforms have been shifted to a common reference before averaging, which is achieved by using retracking results averaged on 1 Hz as new reference range. This shift is achieved by applying an additional phasor after the RCMC and before the range compression. Equivalently, the focused power waveforms can be shifted by non-integer bins via the Fourier shift theorem, but only under the condition that they have been zero-padded by a factor of two in range in order to prevent aliasing.

2.1.2. Comparison of measured 2D IRFs of UF-SAR and FF-SAR

The ocean waveform may be modeled as the triple-fold convolution of the Flat Surface Impulse Response (FSIR), system Impulse Response Function (IRF; also called Point Target Response, PTR) and Probability Density Function (PDF) of the sea surface elevation in the approximation of a non-moving sea surface (Brown, 1977; Ray et al., 2015). The FSIR comprises the instrument's antenna pattern, illumination geometry and surface backscattering properties (Raney, 1998), and so both, the FSIR and the PDF of sea surface elevation are identical for both UF-SAR and FF-SAR. The IRFs account for the instrument's resolution in range and along-track directions. Hence, differences in the UF-SAR and FF-SAR waveform shape are solely due to differences between the IRFs. As such, comparing the IRFs not only helps to assess (dis-) similarities but also allows to gain understanding of why there are differences.

The IRFs can be measured over a transponder, which is a bright, active reflector used for instrument calibration purposes. Theoretical expressions for the IRF have been worked out for UF-SAR (Ray et al., 2015) and FF-SAR (Egido and Smith, 2017; Guccione et al., 2018).

2.1.3. Refinement of 2D IRFs and their impact on ocean waveforms

After comparison of the measured IRF with the theoretical expressions, one can formulate a refined expression for the waveform integral (triple-fold convolution). This allows to discuss the observed similarities and differences in a straightforward manner without explicitly solving the triple-fold convolution. Hence, it enables us to explain the characteristics of averaged ocean waveforms in a simpler framework.

2.2. FF-SAR processing

Our multi-mission FF-SAR processor is a continued development of the CryoSat-2 implementation in Kleinherenbrink et al. (2020a). This processor applies a back-projection algorithm according to the developments of Egido and Smith (2017). It includes the Range Cell Migration Correction (RCMC), the Residual Video Phase (RVP) correction, the Residual Range Phase (RRP) correction, and compensation of additional phase jumps due to altimeter operations (inter-burst jumps, tracker range changes), see Appendix A. On top of that, the satellite missions require some individual settings and adjustments with respect to Kleinherenbrink et al. (2020a), which we also summarize in Appendix A.

2.3. UF-SAR processing

The FF-SAR processor is modified to provide simultaneously the UF-SAR (delay-Doppler) processing results as in Egido and Smith (2017), Egido et al. (2021b): Essentially, the along-track resolution decreases to the UF-SAR case when the coherent integration time is reduced to the burst duration. After the application of all range and phase corrections, one can therefore obtain the ground-steered and range-corrected Doppler-beam-stack by performing a coherent summation within individual bursts, followed by taking the absolute square. Consequently, the multilooked UF-SAR power waveform is obtained from the sum over this stack in azimuth direction. This is illustrated in Fig. 2 for clarity. As shown in the figure all pulse echoes within the whole illumination time T are used in both FF-SAR and UF-SAR processing, although the coherent integration times differ. The coherent integration time of the FF-SAR processor likewise determines the number of bursts in the emulated Doppler beam stack and vice versa.

According to Egido et al. (2021b), the most significant difference between the outlined approach and a conventional delay-Doppler algorithm is that the latter includes a known, small error in the delay-Doppler RCMC (Moreau et al., 2017a; Scagliola et al., 2021; Guccione,
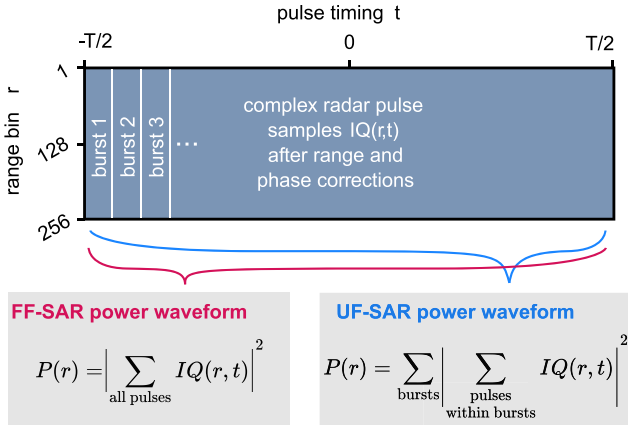
Fig. 2. Differences in forming FF-SAR and UF-SAR power waveforms. $IQ(r,t)$ represents all radar pulses from within the integration time window with length T after application of the focusing, i.e. after RCMC, RVP and RRP corrections.

2008). This error is referred to as 'range walk' and is not intrinsic to UF-SAR processing. The range walk results in some defocusing that slightly widens the power waveforms and thereby introduces a bias of about a decimeter magnitude to the estimated significant wave height (Moreau et al., 2017a; Scagliola et al., 2021). In combination with a drift of S3A altimeter PTR parameters, the range walk contributes also to a spurious drift in global mean sea level (Jugier et al., 2022; Aublanc et al., 2020). We account for this and implement an optional range walk error in our processor, which will be activated only in the comparison to the official EUMETSAT Level-1b product (B).

2.4. Predicted 2D impulse response functions

The waveforms in image space (range r; along-track distance x) obtained in the vicinity of a single point scatterer such as a transponder are called the IRF. The FF-SAR IRF has been approximated by Egido and Smith (2017, Eqs. 25 and 35) and Guccione et al. (2018, Eq. 13) to be

$$h_{\text{FF}}(\eta, \tau_r) \approx \frac{W_B}{W_p} \text{sinc}[B\tau_r]\text{sinc}[W_B\eta]\sum_n \text{sinc}\left[B_{\text{dop}}\left(\eta - \frac{n}{W_p}\right)\right],$$
(1)

with the target located at slow time $\eta \approx x/V_{\text{eq}} = 0$ and range time-delay $\tau_r = 2r/c = 0$. Here, c is the speed of light in vacuum, V_{eq} the ground-projected velocity, B the chirp bandwidth, $B_{\text{dop}} = |FM|T$ the full Doppler bandwidth, $W_B = |FM|T_{\text{burst}}$ the Doppler bandwidth covered by a burst duration, and $W_p = |FM|T_{\text{intra-burst}}$ the Doppler bandwidth corresponding to the burst repetition interval with Doppler rate $|FM|$, as described in the aforementioned references. The Doppler rate can be considered constant over the aperture T in very good approximation (Guccione et al., 2018), hence $|FM| \approx 2f_c V^2(cH)^{-1}$ with satellite velocity V tangential to the surface and tracker range H, see D. After taking the absolute square to get the power of h_{FF}, the resulting cross terms from the sum over n can be safely ignored for

the typical FF-SAR integration times; their relative magnitude is about -30 dB compared to the dominant terms. Expressed in a flat-Earth approximation and using the definitions of τ_r and $|FM|$ above, it can then be shown that the IRF power is proportional to

$$h_{\text{FF}}^2(r,x) = h_{\text{FF}}^2(r)h_{\text{FF}}^2(x) \approx \mathcal{C} \underbrace{\text{sinc}^2\left[\frac{2B}{c}r\right]}_{\text{range sinc with chirp resolution}}$$

$$\times \underbrace{\text{sinc}^2\left[\frac{2T_b f_c V}{Hc}x\right]}_{\text{azimuth sinc with UF-SAR resolution}}$$

$$\times \sum_n \underbrace{\text{sinc}^2\left[T\frac{2f_c V}{Hc}\left(x - n\overbrace{\frac{Hc\text{BRF}}{2f_c V}}^{\text{target copy positions}}\right)\right]}_{\text{repeated azimuth sincs with FF-SAR resolution}},$$
(2)

with burst duration $T_b = N_b/\text{PRF}$, pulse repetition frequency PRF, number of pulses in a burst N_b, carrier frequency f_c, satellite velocity V tangential to the surface, tracker range H, FF-SAR coherent integration time T, and burst repetition frequency BRF. In the remainder of the manuscript, $\mathcal{C}$ is used for constant terms that are of no particular interest. Parameter values for the different SAR altimetry missions are provided in Table 1. The IRF power consists of three terms that describe the range resolution, the along-track UF-SAR envelope, and multiple copies of the target (grating lobes) at FF-SAR resolution in the along-track direction. These grating lobes appear each ~ 90 m for S3 and CS2 due to the closed-burst operation mode, and each ~ 300 m for S6, but only because the quasi-continuous open-burst sampling is interrupted each 64 pulses by a calibration pulse and a C-band pulse for improved ionospheric correction (Donlon et al., 2021). Guccione et al. (2018, see Fig. 8) have stressed that the formulation in Eq. 1 is limited in the sense that it does not describe the inherent blurring of grating lobes in the obtained h_{FF}^2 over a transponder, as the focusing operation is only exact in the focal point at $x = 0$. We will demonstrate in Section 3.3 that this shortcoming forbids to derive a proper ocean waveform model directly from Eq. 1.

The IRF power for UF-SAR does not suffer from grating lobes. Using the expression from Ray et al. (2015, absolute square of Eq. 22) and using all introduced definitions to rewrite the non-dimensional variables, it is approximated by

$$h_{\text{UF}}^2(r,x) = h_{\text{UF}}^2(r)h_{\text{UF}}^2(x)$$

$$\approx \mathcal{C} \underbrace{\text{sinc}^2\left[\frac{2B}{c}\left(r - \frac{\alpha x_l^2}{2H}\right)\right]}_{\text{range sinc with chirp resolution}}$$

$$\times \underbrace{\text{sinc}^2\left[\frac{x - x_l}{L_x}\right]}_{\text{azimuth sinc with UF-SAR resolution}},$$
(3)

where $x_l = L_x l$ is the ground location of the l-th Doppler beam, $L_x = Hc(2T_b f_c V)^{-1}$ and $\alpha = 1 + H/R_E$ with R_E the local radius of curvature of the Earth. To be precise: once evaluating the term $h_{UF}^2(r - R(x,y,z),x)$ with distance $R(x,y,z)$ to a surface element of the ocean surface, one recovers the absolute square of Eq. 22 in Ray et al. (2015). The term $\alpha x_l^2 (2H)^{-1}$ shifts the sea surface into the same range gate among all Doppler beams. It should be stressed that for the zero-Doppler beam ($x_l = 0$) the first two sinc^2 terms are identical for both UF-SAR and FF-SAR (see also Egido and Smith, 2017; Guccione et al., 2018). It needs to be stressed here that the formulation of the IRFs in this section assumes no windowing over the pulse data prior to the UF-SAR and FF-SAR focusing. When a window, e.g. Hamming-window, is applied in fast-time direction (range) prior to the range compression, then the first sinc^2-function in Eqs. 2 and 3 must be replaced with a better functional approximation, e.g. a Gaussian function (Ray et al., 2015). If windowing was applied in slow-time direction (along-track) over each individual bursts, then this would primarily affect the second sinc^2-function in Eqs. 2 and 3, which would need to be replaced accordingly. Therefore, in case of a Hamming window, the power within the closest grating lobes increases, while they are much suppressed further than 600 m away from a target. Full grating lobe mitigation approaches have not yet been developed but are currently investigated by emulating e.g. CS2 and S3 closed-burst sampling with S6 data (Amraoui et al., 2022).

2.5. Sentinel-3 and Sentinel-6 data

For the comparison of averaged FF-SAR and UF-SAR ocean waveforms, we used excerpts of three tracks over the North Sea. To minimize the along-track variation of the SAR waveform shapes, we selected track segments in which the significant wave heights and backscatter coefficients remain rather constant. This was the only requirement for choosing the data. Each excerpt covers approximately one degree of latitude (see Table 2). The unique file identifiers, which include the sensing period and relative orbit and cycle numbers, are provided in

Table 2
Utilized datasets and their key aspects, such as significant wave height (SWH) and backscatter coefficient (SIG0).

case	type	latitude	1 Hz SWH	1 Hz SIG0
S3A-I	ocean	53.5–54.5	1.15–1.85	10.4–10.95
S3A-II	ocean	55–56	4.05–4.9	8.15–8.6
S6A-I	ocean	55.675–56.65	2.05–2.5	17.5–17.75
S3B-TR	transponder	35.338	-	-
S6A-TR	transponder	35.338	-	-

Table 3. The Level-1a (L1a) data were obtained from EUMETSAT's dissemination services via https://eoportal.eumetsat.int, while Level-1b (L1b) and Level-2 (L2) data have been generated by our in–house developed software if not stated otherwise.

Additionally, two transponder overpasses (S3B-TR and S6A-TR) are required over which the IRFs will be measured. The transponder used in this study is deployed in Crete, Greece, at a site called CDN1 Cal/Val. It is located at 35.3379302808 °N, 23.7795182869 °E and 1048.8184 m height with respect to the WGS84 reference ellipsoid (Quartly et al., 2020). The satellite passes over this transponder approximately each 27 days (S3) or 10 days (S6) with across-track distances of typically less than 1 km.

3. Results

This section is organized as follows: In the first part, we compare averaged UF-SAR and FF-SAR ocean waveforms for S3 and S6. We then outline the mission-specific features of the measured two-dimensional radar impulse response functions (2D IRF) over the Crete radar transponder in a second part. Finally, we relate the observations from the first two parts using the triple-fold convolution integral for the average waveform shape.

3.1. Comparison of averaged UF-SAR and FF-SAR ocean waveforms

The integration times for S3 and S6 are 2.1 s and 2 s here, respectively. The normalized averaged waveforms for the data cases S3A-I, S3A-II, and S6A-I (see Table 2) are presented in Fig. 3. The figure also shows the differences between the averaged normalized UF-SAR and

Table 1
List of mission parameters. The values marked with "∼" have been rounded. H and V are varying over the orbit and are mere example values extracted from short track segments. In the case of S6, PRF and BRF vary as well.

variable	CryoSat-2	Sentinel-3	Sentinel-6
tracker range H (km)	∼ 717.24	∼ 805.53	∼ 1344.1
velocity V (km s^{-1})	∼ 7.498	∼ 7.544	∼ 6.97
burst repetition frequency BRF (Hz)	∼ 84.8	∼ 78.53	∼ 139.26
pulse repetition frequency PRF (kHz)	∼ 18.182	∼ 17.825	∼ 9.195
chirp bandwidth B (MHz)	320	320	320
carrier frequency f_c (GHz)	13.575	13.575	13.575
chirp slope s (10^{12} Hz s^{-1})	∼ 7.143	∼ 7.143	∼ 10
number of pulses in burst N_b	64	64	64
burst duration T_b	N_b/PRF	N_b/PRF	N_b/PRF

Table 3
List of EUMETSAT Level-1a unique file identifiers.

| case	file identifier
S3A-I	S3A_SR_1_SRA_A__20211017T101723_20211017T110752_20211112T011946_3029_077_279_____MAR_O_NT_004.SEN3
S3A-II	S3A_SR_1_SRA_A__20211101T102835_20211101T111904_20211127T013420_3029_078_108_____MAR_O_NT_004.SEN3
S6A-I	S6A_P4_1A_HR_____20210901T212456_20210901T222027_20210902T134010_3331_030_018_009_EUM__OPE_ST_F03.nc
S3B-TR	S3B_SR_1_SRA_A__20190620T083403_20190620T092432_20191107T073220_3029_026_335_____MR1_R_NT_004.SEN3
S6A-TR	S6A_P4_1A_HR_____20210901T212456_20210901T222027_20210902T134010_3331_030_018_009_EUM__OPE_ST_F03.nc
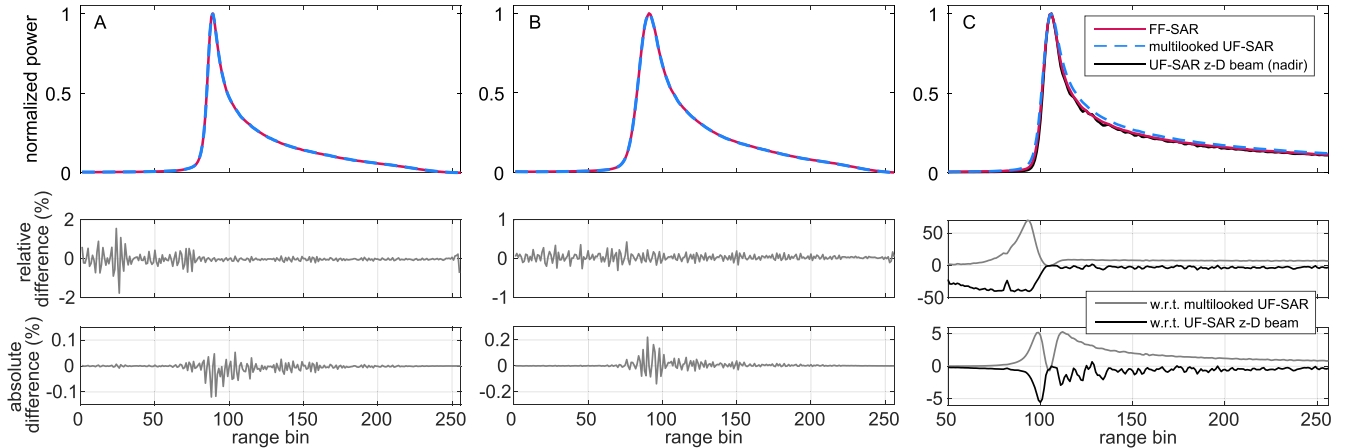
Fig. 3. Top panels show the normalized and averaged ocean power waveforms of UF-SAR (dashed blue line), zero-Doppler beam (solid black line, top right panel only), and FF-SAR (solid red line). Column A shows case S3A-I, column B case S3A-II and column C case S6A-I. For the nadir-looking UF-SAR zero-Doppler beam we accumulated five consecutive Doppler beams closest to nadir for reasons of speckle reduction. These Doppler beams correspond to a Doppler-beam index $l \in [-0.5, 0.5]$, according to Eq. 3. The bottom panels show the relative and absolute differences between the waveforms in the top panel. The relative difference of the normalized waveforms is defined as 100·(UF-SAR - FF-SAR)/FF-SAR [%] and the absolute difference as 100·(UF-SAR - FF-SAR) [%]. The solid grey lines in the bottom panels correspond to differences with the multilooked UF-SAR and the solid black lines to differences with the averaged zero-Doppler beam. To enhance visibility, the right panels only cover range gates 50 to 256.

FF-SAR waveforms. Note that the total integrated powers of the unnormalized UF-SAR and FF-SAR radargrams agreed to approximately 0.02% in all data cases. This is expected because, firstly, both processing methods should conserve the power within the Doppler spectrum and, secondly, the utilized pulse data is identical.

For both S3A-I (Fig. 3A) and and S3A-II (Fig. 3B), we observe a very good agreement between the averaged UF-SAR and FF-SAR waveforms; absolute differences are on the order of 0.25% and relative differences do not exceed the 2% mark.

In the case of S6A-I (Fig. 3C), we observe positive absolute differences of more than 5% around the waveform peak, corresponding to relative differences as high as 65% in the waveforms' foot. The S6 FF-SAR waveforms are indeed narrower than the multilooked UF-SAR ones (as hypothesized by Egido and Smith (2017)), resulting in a steeper leading edge. The comparison in the bottom panels reveals that the S6 FF-SAR ocean waveform is much better resembled by the UF-SAR zero-Doppler beam, particularly in the trailing edge after range gate 100. However, the leading edge is flatter and the foot of the S6 FF-SAR waveform is higher compared to the UF-SAR zero-Doppler beam. The integration time is here reduced to 2 s in order to remove all effects of geometry and ambiguity masking (see Section 7.3.13.4 EUMETSAT, 2022), as they

would have deteriorated the comparison to the zero-Doppler beam. Note that the averaged UF-SAR zero-Doppler beam waveform is somewhat noisier than the multilooked UF-SAR waveform because of the reduced amount of data available to compute the average.

The obtained differences can be attributed to differences between the IRFs of S6 FF-SAR and S3 FF-SAR, and hence, to the different grating lobe positions explained by the open-burst and closed-burst sampling. Steps towards a better understanding are made in the following sections, by analyzing the measured IRFs and inspecting the modeled, averaged waveforms.

3.2. Comparison of UF-SAR and FF-SAR derived IRFs to theoretical models from Section 2.4

Radargrams from two transponder overpasses for S3 and S6 are presented here in comparison to the IRF power $h_{UF}^2(x, r)$ from Eq. 3 for $x_l = 0$ m (zero-Doppler beam). The measured radargrams (power waveforms) over the transponder will be denoted $\mathcal{T}(r, x)$ and referred to as 'transponder image'. The predicted IRFs are separable in the dimensions (r, x), i.e. $h_{UF}^2(x, r) = h_{UF}^2(x)h_{UF}^2(r)$, so that the sum over one dimension does not affect the functional form in the other, e.g.

$$\int \mathrm{dx}\, h_{\mathrm{UF}}^2(x) h_{\mathrm{UF}}^2(r) = C h_{\mathrm{UF}}^2(r). \qquad (4)$$

Therefore, we also provide plots of the marginal transponder images

$$\mathcal{T}(r) = \int \mathrm{dx}\, \mathcal{T}(r,x) \quad \text{and} \quad \mathcal{T}(x) = \int \mathrm{dr}\, \mathcal{T}(r,x),$$

similar in concept to marginal probability distributions, for a rigorous comparison with $h_{\mathrm{UF}}^2(r)$ and $h_{\mathrm{UF}}^2(x)$.

3.2.1. Sentinel-3

The UF-SAR and FF-SAR transponder images are shown in Fig. 4, panels C and F, and Fig. 5. The total integrated power $\mathcal{T}_{\mathrm{tot}}$ of the transponder images $\mathcal{T}_{\mathrm{UF}}$ and $\mathcal{T}_{\mathrm{FF}}$ agrees to about 0.02% due to reasons outlined in the previous section. Particularly in panel C, some secondary targets are visible in the IRF images. These are likely reflections of the transponder target from surfaces around its location, because i) they are much weaker than the main target, ii) they appear later (further away) than the main signal, and iii) they are in focus at about the same along-track distance. We make the following observations:

- **Fig. 4 panels C and F:** The most prominent feature of both transponder images is a bow tie pattern, due to a spread of power in range direction at distances away from the transponder. Although poorly visible at 20 Hz posting rate, the same pattern is present in the

official Level-1b product (not shown). It will be derived in Section 3.3 that this bow-tie pattern is a direct consequence of the multilooking over the whole illumination time.

- **Fig. 4 panel B:** Regardless of this pattern, $\mathcal{T}_{\mathrm{UF}}(x)$ resembles the function $h_{\mathrm{UF}}^2(x)$. $\mathcal{T}_{\mathrm{FF}}(\mathrm{x})$ shows the evenly spaced grating lobes, but these grating lobes become blurred in azimuth and range with increased distance from the transponder, best to see in the enlarged view in Fig. 5. This has already been observed by Guccione et al. (2018, compare to Figs. 8 and A1). We will later show that the effect appears less pronounced in their work because only 25% of the Doppler bandwidth (integration time of less than 1 s) was used. As illustrated by the transparent red dots, the integrated peak power of the grating lobes of $\mathcal{T}_{\mathrm{FF}}(x)$ (determined from a moving sum) is still modulated by $h_{\mathrm{UF}}^2(x)$. Indeed, this is regardless of the observed blurring.

- **Fig. 4 panels D, E, G and H:** Due to the bow tie pattern, the integrals $\mathcal{T}(r)$ significantly vary from the term $h_{\mathrm{UF}}^2(r) = h_{\mathrm{FF}}^2(r)$: The resulting $\mathcal{T}_{\mathrm{UF}}(r)$ and $\mathcal{T}_{\mathrm{FF}}(r)$ are similar and considerably flatter and wider than the prediction.

3.2.2. Sentinel-6

Here we repeat the same analysis for a transponder overpass of S6, see Fig. 6. Very similar observations can be made, except for a few important differences:
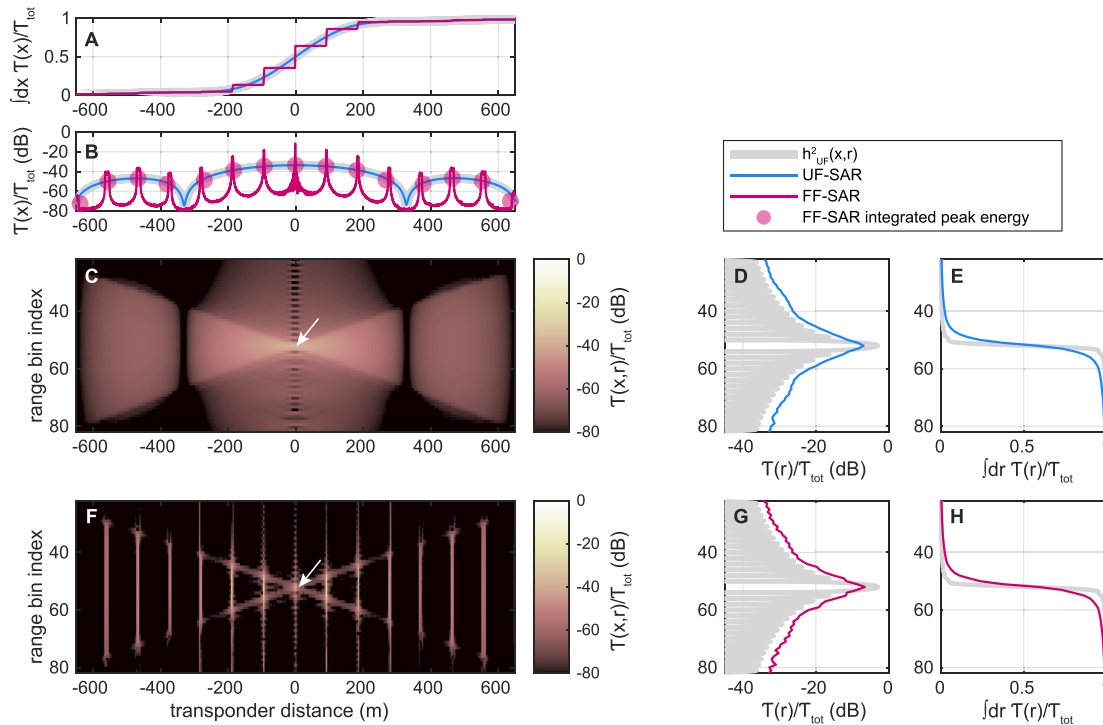

Fig. 4. Panels C and F show excerpts of the UF-SAR and FF-SAR transponder images $\mathcal{T}(x,r)$ from case S3B-TR. The white arrows mark the transponder position. The integrated, marginal functions $\mathcal{T}(x)$ and $\mathcal{T}(r)$ are plotted in the panels B, D and G, above and next to the IRF images and are accompanied by the functions $h_{\mathrm{UF}}^2(r) = h_{\mathrm{FF}}^2(r)$ and $h_{\mathrm{UF}}^2(x)$ (in grey). To show how the power is spread along the two dimensions on linear scales, we additionally provide the indefinite integrals of $\mathcal{T}(x)$ and $\mathcal{T}(r)$ in the panels A, E and H, similar in concept to a cumulative distribution function.
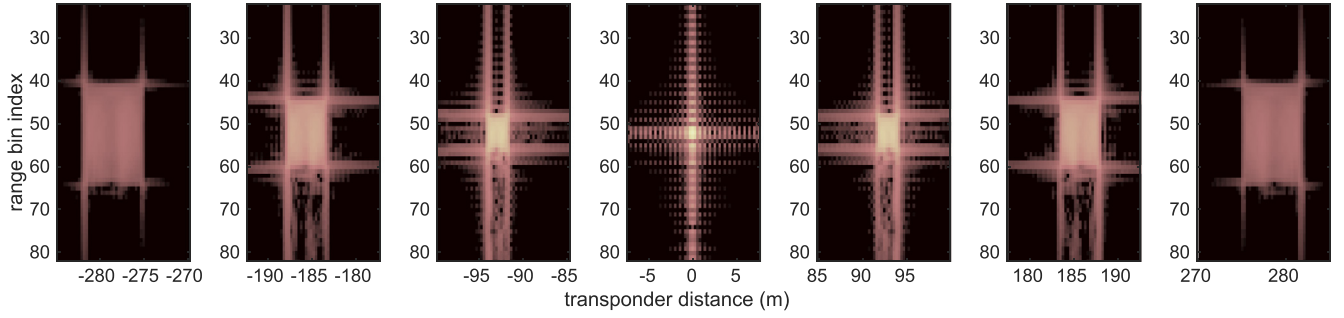
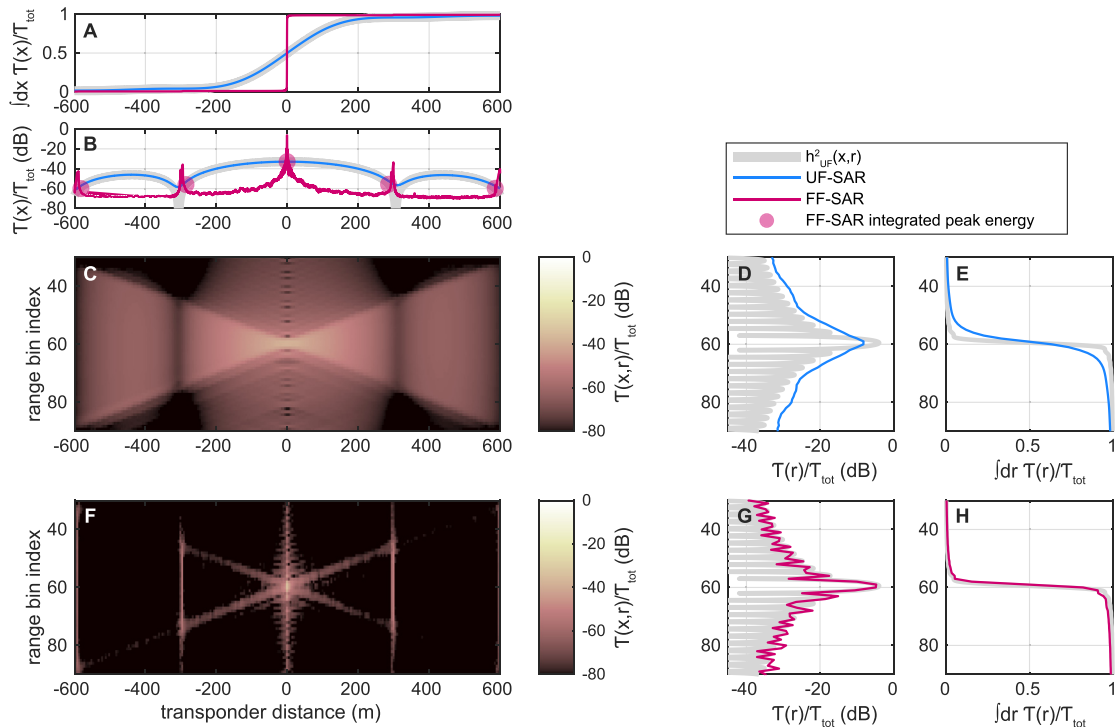Fig. 5. Enlarged view of S3B-TR transponder image from panel F of Fig. 4.

Fig. 6. Same as Fig. 4 for case S6A-TR.

- **Fig. 6 panel B:** The measured $\mathcal{T}_{\mathrm{UF}}(x)$ does not dip as far as predicted at the zeroes of $h_{\mathrm{UF}}^2(x)$. At least one reason for this can be the varying PRF of S6, which slightly changes the along-track resolution from burst to burst and hence blurs the UF-SAR transponder image in along-track direction, once several Doppler beams are being multilooked. The grey curve in the figure assumes a constant PRF, obtained from the median in the data file. The FF-SAR grating lobes appear close to the minima of the UF-SAR envelope $\mathcal{T}_{\mathrm{UF}}(x)$ and therefore contain much less power compared to the case of S3.

- **Fig. 6 panels D, E, G and H:** The negligible S6 FF-SAR grating lobe power causes that $\mathcal{T}_{\mathrm{FF}}(r)$ is much peakier than $\mathcal{T}_{\mathrm{UF}}(r)$ and very well described by the prediction $h_{\mathrm{UF}}^2(r) = h_{\mathrm{FF}}^2(r)$, as only the FF-SAR main lobe contributes significantly to the total power.

The marginal functions $\mathcal{T}(r)$ are intuitively expected to have significant influence on the waveform shape, as they express how the power of a single scatterer on the sea surface is imaged in the range dimension. The differences between $\mathcal{T}_{\mathrm{FF}}(r)$ in Figs. 4 and 6 therefore provide a first insight to the observations made in Section 3.1. The range-smearing of the grating lobes was identified to have major influence on $\mathcal{T}(r)$, but this blurring is not described by Eq. 2. This makes a refinement necessary, which will be derived in the following section.

3.3. Refinement of 2D IRFs and their impact on ocean waveforms

Following the approach in Ray et al. (2015, Eq. 23), we can write the average backscattered power waveform as

$$W_c(r) \approx \mathcal{C} \int \mathrm{d}z \, p(z)$$
$$\times \int \mathrm{d}y \int \mathrm{d}x \frac{G^2(x,y)\sigma_0(x,y)}{r^4} h_c^2(r - R(x,y,z),x),$$
$$(5)$$

where G is the antenna pattern, σ_0 the radar cross section, c marks either the UF-SAR or FF-SAR case, and R the range from satellite to the surface element at (along-track distance x, cross-track distance y, and height z). The integration is performed with the limits $-\infty$ to ∞ (over the whole radar footprint). In the UF-SAR case, the term $h_{\mathrm{UF}}^2(r - R(x,y,z),x)$ is entirely equivalent to the absolute square of Eq. (22) in Ray et al. (2015). Making the approximations that the radar cross section σ_0 and r^4 are slowly varying functions (σ_0 is commonly considered constant over open ocean) and using that the antenna pattern can be split via $G(x,y) = G_x(x)G_y(y)$ yields

$$W_c(r) \approx \mathcal{C} \int \mathrm{d}z \, p(z) \int \mathrm{d}y \, G_y^2(y)$$
$$\times \int \mathrm{d}x \, G_x^2(x) h_c^2(r - R(x,y,z),x) \qquad (6)$$

similar to Eq. 30 in Egido and Smith (2017). If the predicted IRF from Eq. 1 was correct, this expression would readily compute the average power waveform for the FF-SAR case. We have shown in the previous Section 3.2 that this is not the case. For UF-SAR, however, this expression does not yet capture the multilooking over all available Doppler beams. Indeed, normally the individual Doppler beam waveform models are summed up within the retracking process (Ray et al., 2015; Dinardo, 2020) allowing to account for varying orbit parameters within the illumination time. In the following, we will take a different but equivalent route, namely by multilooking all l Doppler beam contributions $h_{\mathrm{UF}}(r,x;x_l)$ prior to the integration in Eq. 6. This yields an approximate, closed-form analytical expression for better comparison of the averaged FF-SAR waveforms with the multilooked UF-SAR waveforms.

3.3.1. Multilooked UF-SAR case

To keep a good trade-off between readability and insight, the following derivations are made in, but not limited to, the flat-Earth approximation and under assumption of constant tangential velocity of the satellite with respect to the surface within the illumination time. The latter makes the problem translational invariant, i.e. steering a Doppler beam from a burst at time $t_b = 0$ to an along-track position $x = x_l$ is the same as steering a Doppler beam from a burst at time $t_b = -x_l/V$ to position $x = 0$. Given the burst timings $t_b \in [-T/2, T/2]$, all non-integer Doppler beams with $x_l = L_x l = V t_b$ contribute to the multilooked UF-SAR waveform. As mentioned above, the multilooked UF-SAR waveform is obtained from summation of Eq. 6 over all Doppler beams (equivalently burst timings)

$$W_{\mathrm{UF}}^{\mathrm{multi}}(r) = \sum_{t_b} W_{\mathrm{UF}}(r)$$
$$\approx \mathcal{C} \int \mathrm{d}z \, p(z) \int \mathrm{d}y \, G_y^2(y)$$
$$\times \int \mathrm{d}x \underbrace{\sum_{t_b} G_x^2(x) h_{\mathrm{UF}}^2(r - R(x,y,z),x;x_l = V t_b)}_{= I_{\mathrm{UF}}(x,y,z)},$$
$$(7)$$

where the sum has been pulled into the integrals using the linearity of integration, which defines the integrand $I_{\mathrm{UF}}(x,y,z)$. We may shift each summand of I_{UF} via $x \to x + V t_b$ for the reason of translational invariance, without changing the integral. With a parabolic (second-order) approximation of $R(x + V t_b, y, z)$ over the footprint and Eq. 3, one then obtains

$$I_{\mathrm{UF}}(x,y,z) \to \mathrm{sinc}^2\left[\frac{x}{L_x}\right] \sum_{t_b} G_x^2(V t_b + x)$$
$$\times \mathrm{sinc}^2\left[\frac{2B}{c}\left(r - r_0(y,z) - \left(\frac{xV}{H}t_b + \frac{x^2}{2H} - \frac{xf_c V}{Hs}\right)\right)\right]$$
$$= \mathcal{T}_{\mathrm{UF}}(r - r_0, x), \qquad (8)$$

with range offset $r_0(y,z) = y^2(2H)^{-1} - z$ and chirp slope s. For a discussion on the validity of this assumption, we refer to the Appendix C. We recall here that the Doppler beams point towards the target from different satellite positions. Therefore the summands happen to be scaled by the antenna pattern as function of the look angle (Scagliola et al., 2015), or equivalently ground distance. For this reason, the integrand $I_{\mathrm{UF}}(r,x)$ can be identified as the actual transponder image $\mathcal{T}_{\mathrm{UF}}(r,x)$ as seen in the multilooked power waveforms. The first term of $\mathcal{T}_{\mathrm{UF}}(r,x)$ equals the along-track part of the IRF $h_{\mathrm{UF}}^2(x;x_l = 0)$ for the zero-Doppler beam. However, the second term resembles a summation of mutually displaced range IRFs $h_{\mathrm{UF}}^2(r)$. Hence, an along-track distance x away from the target, the power in the multilooked waveforms is smeared over a total range xVT/H. Hence, this expression reproduces the bow-tie pattern observed in the transponder overpasses. This smearing occurs because the RCMC applied at focus points $x \neq 0$ is not strictly correct for a target at $x = 0$. The modeled $\mathcal{T}_{\mathrm{UF}}(r,x)$ is plotted in Figs. 7 and 8, showing good qualitative agreement with the observations made in Section 3.2. It is a meaningful result that the range-smearing is linearly dependent on the total time used for multilooking, i.e. the integration time T. Similarly, the SAMOSA model waveform becomes wider the more Doppler beams are included for multilooking.

In a second step, one can argue with translational invariance that the integral for the marginal transponder image

$$\mathcal{T}_{\mathrm{UF}}(r - r_0) = \int \mathrm{d}x \, \mathcal{T}_{\mathrm{UF}}(r - r_0, x) \qquad (9)$$

resembles the power waveform that would be obtained over an along-track line of uniform scatterers at a distance
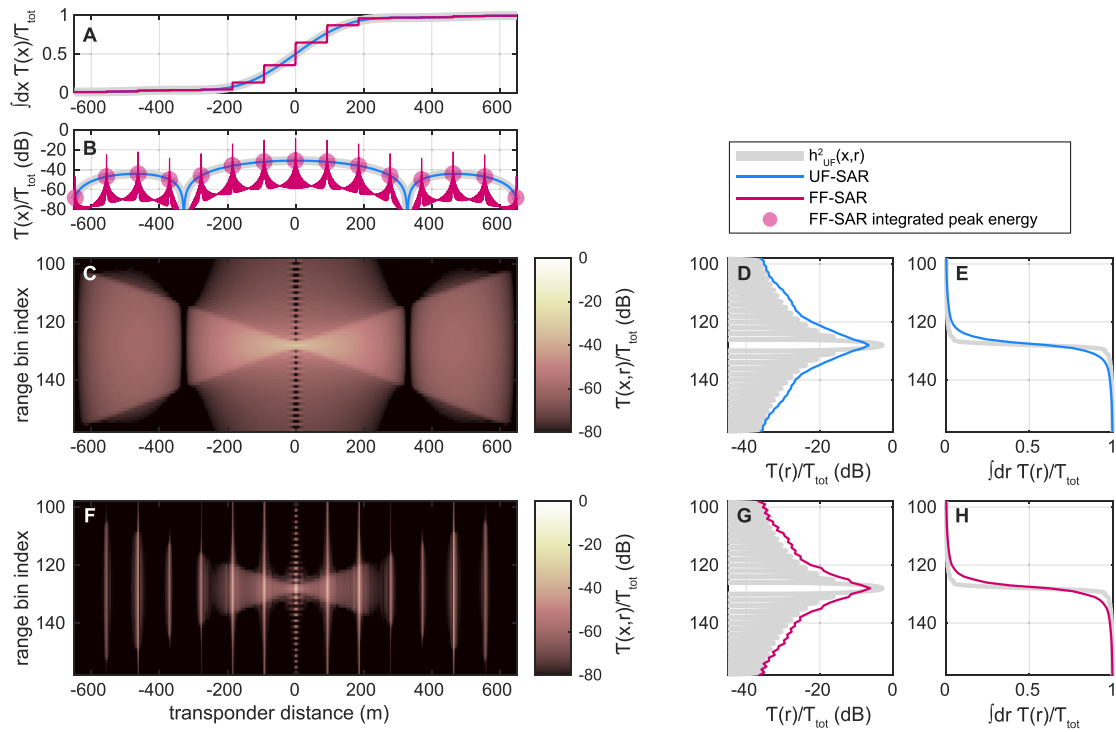
Fig. 7. Same as Fig. 4, but showing the S3B IRF models instead of measurements. Panels C and F show Eqs. 8 and 13, generated with the orbit parameters of the transponder test case S3B-TR.
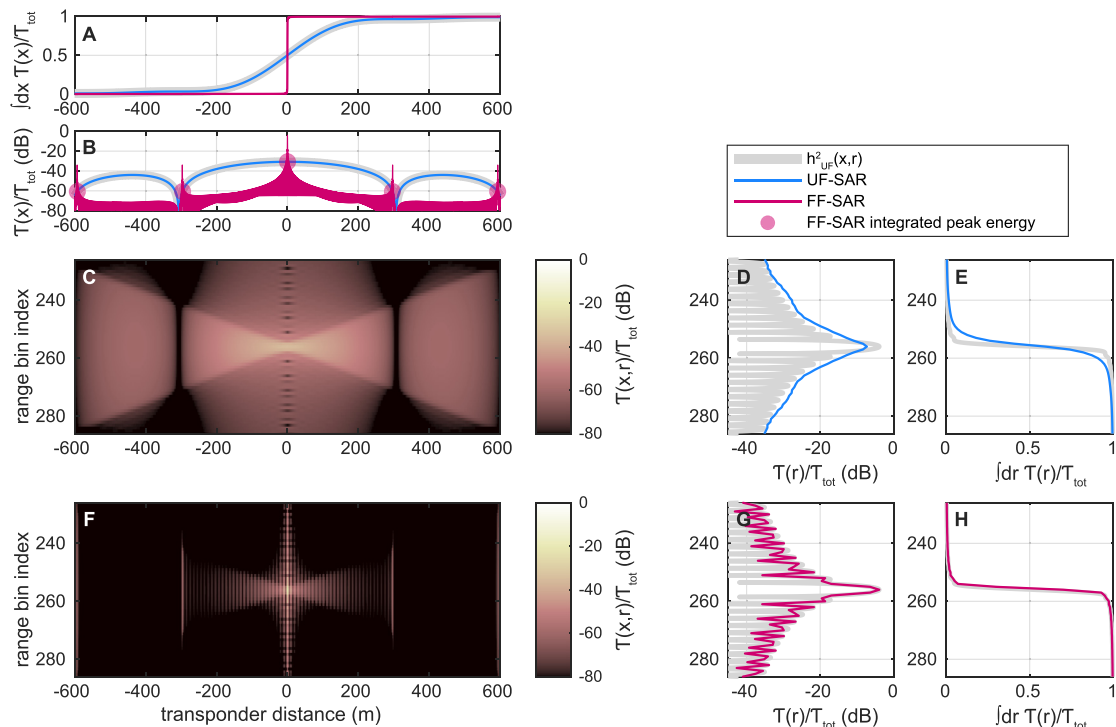

Fig. 8. Same as Fig. 7 but with parameters from test case S6A-TR.

$r_0(y, z)$ away from the satellite. Note that in the following, dropping the dependent variable x implies that this variable has been integrated over. Referring to the radar flat surface response, which is obtained from the convolution of IRF and FSIR, we refer to the integral $\mathcal{T}_{UF}(r - r_0)$ as 'multilooked radar flat-line response'. It should be noted that the multilooked power waveform is related to the multilooked radar flat-line response via the convolution

$$W_{\text{UF}}^{\text{multi}}(r) \approx C \int dz p(z) \int dy G_y^2(y) \mathcal{T}_{\text{UF}}(r - r_0(y, z)). \quad (10)$$

Hence, the waveform model can be thought of as 2D integral of line scatterers through the (y,z)-plane, which are weighted according to the squared across-track antenna pattern and the height distribution of scatterers.

3.3.2. FF-SAR case

We have derived above that the characteristic bow tie pattern is a purely geometrical consequence of varying satellite looking angles over the illumination time T. Hence, the same effect should be present for FF-SAR. For the derivation of the 2D FF-SAR IRF, it is assumed in Egido and Smith (2017) that only the RRP changes when focusing an along-track distance x away from the target. While this is a valid assumption around the narrow main lobe, the differences in RVP and RCMC become significant for the grating lobes. In fact, it can be shown that the difference between the applied RCMC at along-track distance x away from the target and the required RCMC for that target at $x = 0$ is approximated by

$$\Delta R_{rcmc}(t_p; x) \approx \left[\frac{Vx}{H}\right] t_p + \left[\frac{x^2}{2H} - \frac{xf_cV}{Hs}\right] \quad (11)$$

over a flat Earth, see Appendix C. Here we denote by $t_p \in [-T/2, T/2]$ the relative pulse timing w.r.t. nadir. This effect has been qualitatively described in Buchhaupt et al. (2021, see Appendix A.3). It is worth recalling here that the very same expression appears in the multilooked UF-SAR case, see Eq. 8, for natural reasons: Any range misalignment within the incoherent UF-SAR multilooking is equally present before the coherent summation of the radargram for FF-SAR, compare Figs. 2 and 9, showing how the sinc-shaped range responses of all pulses are offset with respect to each other in case of non-zero along-track distance x. Given that a target is located at any off-nadir grating lobe position, its power will be smeared in range direction by the same amount as in the UF-SAR multilooked transponder image. Assuming that this range misalignment for grating lobe targets does not crucially affect the FF-SAR along-track focusing, we similarly obtain

$$W_{\text{FF}}(r) \approx C \int dz p(z) \int dy G_y^2(y)$$
$$\times \int dx \mathcal{T}_{\text{FF}}(r - r_0(y, z), x), \quad (12)$$

with

$$\mathcal{T}_{\text{FF}}(r - r_0, x) = h_{\text{FF}}^2(x) \sum_{t_p} G_x^2(Vt_p + x)$$
$$\times \text{sinc}^2 \left[\frac{2B}{c}\left(r - r_0(y, z) - \left(\frac{xV}{H}t_p + \frac{x^2}{2H} - \frac{xf_cV}{Hs}\right)\right)\right] \quad (13)$$
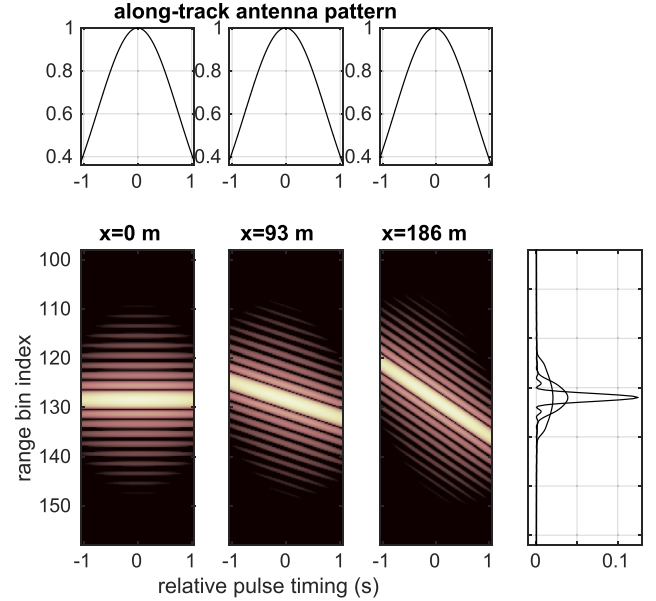

Fig. 9. Simulated radar pulse echoes (absolute squared) corresponding to Fig. 2 obtained with a point target at along-track position x after RCMC, according to the predicted RCMC residual from Eq. (11). The targets at off-nadir positions have another range history and are therefore not perfectly aligned before the multilooking (in UF-SAR case) and before the coherent summation (in FF-SAR case).

where $h_{\text{FF}}(x)$ is the along-track part of the FF-SAR IRF, as in Eq. 2. The validity of this approach is governed by two reasons: i) the total power in the grating lobes has been found to agree with h_{FF}^2 regardless of the defocusing in along-track direction, and ii) this along-track blurring by several meters has only marginal influence on the result of the integral $\int dx$ over the same dimension. The obtained modeled transponder images are provided in Figs. 7 and 8. It needs to be stressed that the considerations above ignore all wave motion effects, as opposed to Buchhaupt et al. (2021): the movement of the sea surface effectively causes additional blurring of the function $h_{\text{FF}}(x)$ with the probability density function (PDF) of the vertical velocity component, resulting in a lowered along-track resolution and a somewhat smoothened flat line response function. The reason to neglect these effects in first order is the same reason for which we ignore the along-track defocusing of the stationary target.

The full potential of the (multilooked) flat-line response functions $\mathcal{T}(r - r_0)$ is unveiled by comparing the expressions 10 and 12. Indeed, in this approximation any difference in between the UF-SAR and FF-SAR waveforms is exclusively caused by the differences between the much simpler functions $\mathcal{T}_{\text{UF}}(r - r_0)$ and $\mathcal{T}_{\text{FF}}(r - r_0)$, allowing statements about the waveform shapes without involving complicated integrals. In a first step, we check whether the theoretically derived and the measured $\mathcal{T}(r - r_0)$ agree with each other.

Fig. 10 shows the measured flat line responses $\mathcal{T}(r - r_0)$ from Section 3.2 in comparison to the modeled ones from
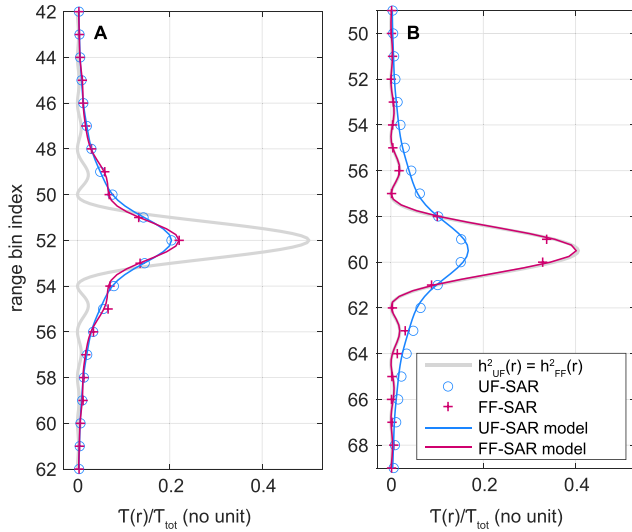
Fig. 10. Comparison of transponder images from Figs. 4 and 6 with IRF models from Eqs. 8 and 13 in terms of the flat line response $\mathcal{T}(r - r_0)$ for Sentinel-3 (panel A) and Sentinel-6 (panel B). The range offset r_0 was manually adjusted to represent the data best. Differences between UF-SAR and FF-SAR ocean waveforms are entirely governed by differences between these functions, when sea surface motion is neglected. The legend regards both panels.

Eqs. 8 and 13, indicating good agreement between the observations and the theoretical formulation. While the flat line responses are similar in FF-SAR and UF-SAR for S3, they differ greatly for S6. The significance of this result is that it predicts similar waveform shapes in FF-SAR and UF-SAR for S3. The remaining oscillations of $\mathcal{T}_{FF}(r)$ around $\mathcal{T}_{UF}(r)$ will be drastically smoothened by the convolution in 10. However, the high-frequency residuals in Figs. 3A and 3B are a relict of this. The second insight is that S6 FF-SAR waveforms ought to be narrower than the UF-SAR waveforms. This is due to the weak grating lobes in the S6 FF-SAR IRF, which are also range-smeared but fall approximately into the zeros of the along-track envelope (second term in Eq. 2).

It is worth recalling here also the theoretical results in Egido and Smith (2017) that if only the FF-SAR main lobe was considered, then the FF-SAR waveform shape resembled the UF-SAR zero-Doppler beam (single look) waveform. For S6, ΔR_{rcmc} has a magnitude of about 5 mm for the FF-SAR main lobe, and 1.5 cm for the UF-SAR zero-Doppler beam. Therefore it is neglectable over the along-track integrals $\int dx$ for these cases. In line with what has been reported we would then obtain

$$W_{UF}^{ZD}(r), \; W_{FF}^{ML}(r) \approx \mathcal{C} \int dz\, p(z)$$
$$\times \int dy\, G_y^2(y)\, \text{sinc}^2\left[\frac{2B}{c}(r - r_0(y, z))\right] \tag{14}$$

for UF-SAR zero-Doppler beam (labeled ZD) and FF-SAR main lobe (labeled ML) after pulling all constants out of the integral. The proportionality constants differ, which must be considered for the estimation of σ_0 with FF-SAR by the established SAMOSA model. However, this result is only useful in case the grating lobes are completely ignored. This is only approximately the case in S6, as the grating lobes still contain about 1% of the total power. Besides wave motion, this provides another reason why the S6 FF-SAR waveform foot is bigger than for UF-SAR zero-Doppler beam in Fig. 3C.

The considerations in this section enabled us to model the transponder images from the previous section. But more importantly, these insights provide an explanation for the unexpected (dis-) similarities of averaged UF-SAR and FF-SAR ocean waveforms from Section 3.1.

3.4. UF-SAR emulation strategy for S6

From the S6 flat line responses in Fig. 10 and the theoretical findings in Section 3.3, we see that $\mathcal{T}_{UF}(r)$ is essentially a blurred version of $\mathcal{T}_{FF}(r)$ for S6 due to the range-smearing. This, and the fact that the total power of both UF-SAR and FF-SAR radargrams was found to agree, suggests that both functions can be linked via a unit-power convolution kernel $K(r)$ via

$$\mathcal{T}_{UF}(r) = K(r) * \mathcal{T}_{FF}(r)$$
$$\iff \quad K(r) = \mathcal{F}^{-1}\left\{\frac{\mathcal{F}\{\mathcal{T}_{UF}(r)\}}{\mathcal{F}\{\mathcal{T}_{FF}(r)\}}\right\}, \tag{15}$$

utilizing the Discrete Fourier Transform $\mathcal{F}$ to obtain $K(r)$ via the classical Fourier deconvolution approach. Equivalently, it allows to emulate a S6 UF-SAR waveform shape from the FF-SAR waveform via the convolution $K(r) * W_{FF}(r)$. We address the limitations of this approach in the end of this section and the discussion. $K(r)$ can be calculated semi-analytically from the data in Fig. 8, which show the functions $\mathcal{T}(r, x)$ from Eqs. 8 and 13. We applied the kernel to the FF-SAR ocean waveforms of case S6A-I and obtain the results in Fig. 11. Regardless of the involved approximations, the application of the convolution kernel reduces the absolute differences between multilooked UF-SAR and FF-SAR waveforms to a mere fraction of about 0.5% and leaves a maximum relative difference of about 8% in the waveform's foot. This result is both appreciable and considerable, because it suggests that established UF-SAR retracking methods could be applied to S6 FF-SAR waveforms, given that the waveforms were pre-processed accordingly.

Fig. 12 shows the SWH estimates for the case S6A-I obtained using different processing and retracking strategies. In particular, we provide SWH estimates from FF-SAR data by using i) the SAMOSA2 zero-Doppler beam as waveform model, and ii) by applying the full SAMOSA2 model to the convoluted (range-smeared)FF-SAR waveforms. Also provided are estimates from UF-SAR waveforms with and without simulated range-walk effect
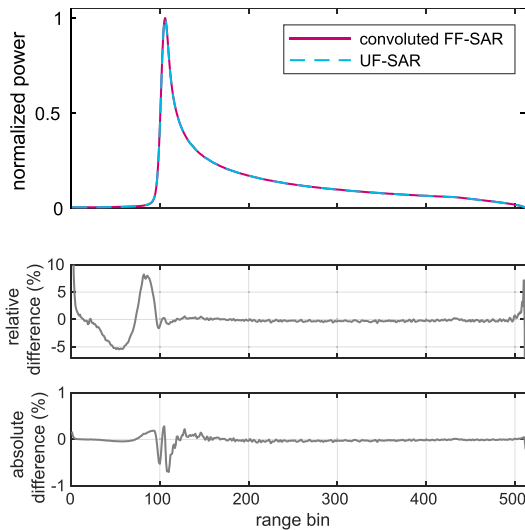
Fig. 11. Same as Fig. 3A for test case S6A-I, including the convolution of FF-SAR waveforms with the kernel K from Eq. 15.
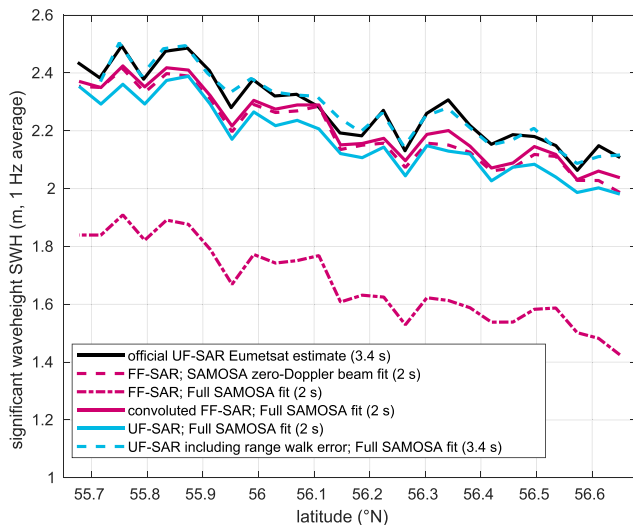

Fig. 12. Estimated significant wave height averaged to 1 Hz for the data case S6A-I over open ocean, following different processing strategies. The used integration times T are indicated in the legend. The Full SAMOSA model includes all Doppler beams from all bursts within the respective integration times.

(Guccione, 2008). The full SAMOSA2 model refers to the SAMOSA2 model that includes all Doppler beams from all bursts within the respective integration time. The same alpha look-up-table (LUT Dinardo, 2020) is being used for both, the full SAMOSA2 model and the SAMOSA2 zero-Doppler beam fit. The results show that naively applying the full SAMOSA2 model to S6 FF-SAR data results in a bias of about -0.5 m. All other SWH estimates lie roughly within a ± 10 cm band around the official data product. Moreover, the parameters from UF-SAR (2 s, solid blue) and convoluted FF-SAR (2 s, solid red) retracked by the full SAMOSA2 model agree to about 6 cm with each other, but are about 6–12 cm lower than

the official estimate. However, a good part of these differences with the official product can be accounted to the range-walk effect, as a separate run of UF-SAR with simulated range-walk and 3.4 s illumination time shows (dashed blue). Direct fitting of the SAMOSA zero-Doppler beam to S6 FF-SAR waveforms (dashed red) results here in a slight overestimation of a few centimeters with respect to the corresponding UF-SAR results. It was stressed already in Section 3.3 that this approach does fully ignore the grating lobes, which widen the waveforms. Thus, a positive SWH bias with respect to the other processing strategies was expected. This SWH comparison claims not to be extensive, but serves as an illustrative asset for all considerations above.

Note that the UF-SAR emulation strategy should be considered a workaround for testing and comparison purposes, as it involves additional approximations and may hence increase the margin of error. It must also be stressed that this convolution approach is a pure emulation strategy to map the waveform shapes onto each other, while the benefit of FF-SAR along-track resolution remains. This aspect is illustrated with the segment of S6 data shown in Fig. 13, which contains clutter from vessels within the ocean waveforms. Regardless of the convolution in range, any coherent targets are imaged with high azimuth resolution as opposed to UF-SAR. The effect of the convolution kernel $K(r)$ is a smoothing of the signal along the range direction in order to widen the FF-SAR waveforms. This is clearly visible in the comparison.

3.5. SSH and SWH retracking

We have analysed the waveform statistics of S3 and S6 and identified the main cause for the differences between UF-SAR and FF-SAR waveforms. In order to check those findings for consistency, we apply SAMOSA2 retracking to the data cases S3A-I and S6A-I (ocean). As our processing chain has not been validated/calibrated for calculation of sigma0, we report here only results for sea surface height (SSH) and significant wave height (SWH). The main objec-
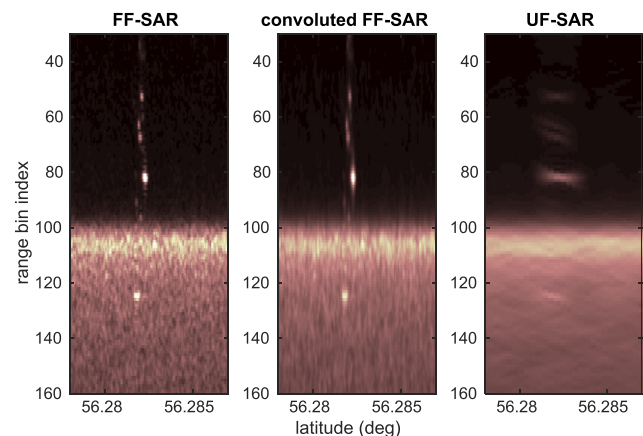

Fig. 13. Example of waveform contamination with S6.

tive is to evaluate if there is a significant bias between the retracking results of UF-SAR and FF-SAR.

The results for S3, using the identical SAMOSA2 retracker with all Doppler beams, are presented in Fig. 14. No significant biases are found over the analysed segment and the correlation exceeds 0.9, in line with the findings regarding the S3 waveform shapes in preceding sections.

For S6, we retrack the FF-SAR waveforms using only the zero-Doppler beam of the SAMOSA2 model. The results are shown in Fig. 15 and indicate no significant range bias over the segment, while the FF-SAR SWH is biased by about 5 cm in this case. The SWH correlation coefficient of 0.84 is slightly lower than for the S3, which can be accounted to the different along-track speckle noise autocorrelations of multilooked FF-SAR and UF-SAR due to their very dissimilar IRFs.

It must be stressed that with the limited data considered, a range bias of FF-SAR vs. UF-SAR of about 1–2 mm is possible for both of the approaches and can only be disconfirmed and analysed for sea state dependencies with help of a much larger dataset, which is not within the scope of this work.

4. Discussion

To gain understanding of the unfocused and focused return signals (power waveforms), we derived a model for the 2D IRF including the effects of range smearing due to an imperfect RCMC correction. In doing so, we relied on the following approximations: i) constant σ_0 over the footprint, ii) a constant velocity V and parabolic range history iii) constant integration time in the FF-SAR case over all range bins and iv) no sea surface motion. These are addressed in the following.

If not constant, σ_0 is commonly modeled with Gaussian dependence upon incidence angle (Brown, 1977; Dinardo, 2020; Buchhaupt et al., 2021), whose width relates to the mean square sea surface slope. As such, it can be split into $\sigma_0(x, y) = \sigma_{0,x}(x)\sigma_{0,y}(y)$ and absorbed into the antenna pat-

Fig. 14. Retracking results of FF-SAR and UF-SAR for data case S3A-I. The FF-SAR data has been multilooked (averaged) at 80 Hz prior to retracking. The biases with 95% confidence interval and the correlation coefficient R are reported in the panels.
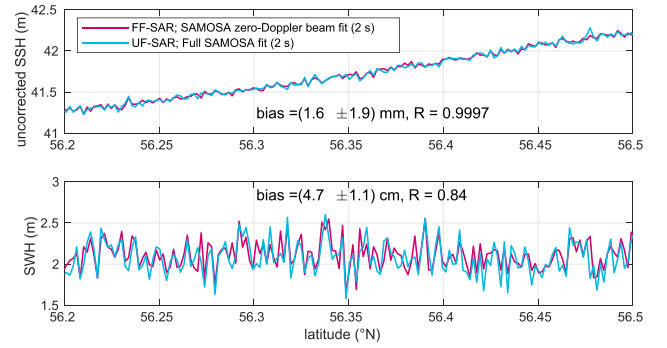

Fig. 15. Retracking results of FF-SAR and UF-SAR for data case S6A-I. It has been stressed by Kleinherenbrink et al. (2020a) how too high speckle noise can bias the retracked range, and hence SSH. Therefore, the FF-SAR data has been multilooked (averaged) at 20 Hz prior to retracking. As opposed to Fig. 14 (80 Hz), this 20 Hz average is required for sufficient noise-suppression, due to the reduced speckle noise resolution of S6 FF-SAR with 2 s illumination time on the one hand and due to the lacking range smoothing (inherent to S3 FF-SAR, previous section) on the other. The biases with 95% confidence interval and the correlation coefficient R are reported in the panels.

tern. That is, one simply replaces $G_i^2(i)$ with $G_i^2(i)\sigma_{0,i}(i)$ for $i = x, y$ in Section 3.3.

The approximation of constant velocity is common and not critical. Guccione et al. (2018) used it to derive a computationally more efficient focusing algorithm that was shown to have similar performance. The range history to the target $R(x, y, z)$ is typically approximated by a 4th-order polynomial fit to the satellite geolocation data (Egido and Smith, 2017) to ensure proper focusing for FF-SAR and the exact satellite location at each burst is utilized to build the Doppler beam stack in the delay/Doppler processing for UF-SAR (Dinardo, 2020). To derive the 2D IRF model in Section 3.3, we have used a parabolic second order polynomial range history, resulting in deviations of up to 4 mm at high pitch angles. This is neglectable compared to the range resolution on the order of several decimeters. Note, however, that one can derive Eq. 8 using an alternative approximation of $R(x, y, z)$. Fig. 10 indicates that the achieved agreement between approximated flat line responses and the transponder measurements is sufficient for the objective of this work.

The furthermost range gates are sampled over a shorter integration time than, e.g., the leading edge (see e.g. Guccione et al., 2018; Kleinherenbrink et al., 2020b; Buchhaupt et al., 2021). This goes hand in hand with a lowered along-track resolution of FF-SAR in these bins. It has also been demonstrated that a shorter illumination time leads to less range-smearing. This has as consequence that the expressions $\mathcal{T}$ from Eqs. 8 and 13 are implicitly dependent on the range to the scatterer, because the illumination time T is reduced with increasing cross-track distance r_0. Therefore, also the proposed kernel $K(r)$ is altered for the furthermost range gates. This can be accounted for by evaluating $K(r)$ for different integration times, but affects only the last 100 range gates in the test case S6A-
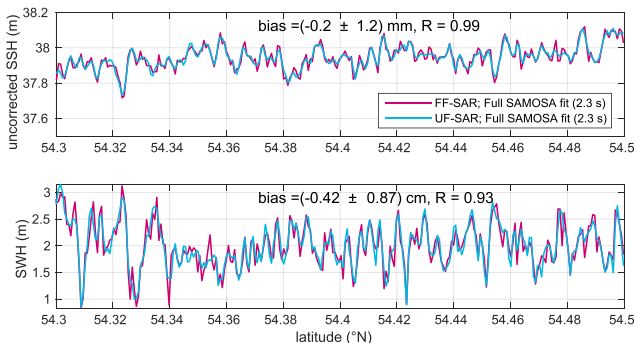
I, where an integration time of 2 s was chosen. Generally, disregarding this dependence is of little consequence where the waveform is very flat, as it is the case in the trailing edge.

Sea surface motion impacts SAR altimetry data in two ways. First, long swell waves undulate on longer scales than the effective altimeter resolution, thus harming the approximation of a Gaussian sea surface distribution in SAR mode retrackers and introducing coloured noise on geophysical estimates (Moreau et al., 2018; Rieu et al., 2021b). Swell waves can hence introduce significant distortions to SAR altimeter radargrams (see also Altiparmaki et al., 2022), but are out of scope of this study as we aimed to understand the averaged waveform shapes. Second, the effect of sea surface motion alters the Doppler frequency of scatterers. Therefore, scatterers moving upwards and downwards within the SAR footprint are virtually shifted forward or backward in azimuth direction, thus causing an azimuth blur (Alpers and Rufenach, 1979; Boisot et al., 2016; Buchhaupt, 2019; Egido and Ray, 2019). Both effects are not present in pulse-limited (Pseudo) Low Resolution Mode (PLRM) due to an isotropic footprint of several kilometers in diameter and the absence of Doppler processing. First and foremost, the wave motion (vertical velocity variance) degrades the azimuth resolution by blurring the IRF. But it also widens the UF-SAR and FF-SAR waveforms which is indistinguishable from effects of significant wave height for both UF-SAR and FF-SAR retrackers (Buchhaupt, 2019; Buchhaupt et al., 2021). Our derivations in Section 3.3 illustrate this conceptually, by showing how a blurring in the along-track IRF $h(x)$ can cause a widening of the waveform in range, because different parts of the bow tie pattern become focused. This causes that the SAR mode derived SWH exhibits a sea state dependent bias compared to the PLRM SWH and in situ measurements for CS2, which becomes as high as 30 cm for a SWH of 6 m (Moreau et al., 2017b; Moreau et al., 2018; Abdalla et al., 2018; Buchhaupt, 2019). Similar trends have been found for S3 (Moreau et al., 2017b; Raynal et al., 2018). This bias becomes smaller with increasing wavelengths and was therefore traced back to be caused mainly by wave motion alone (Amarouche et al., 2019; Egido and Ray, 2019; Buchhaupt, 2019) as longer waves show lower orbital velocities. However, our results indicate that the velocity variance induced widening ought to be similar in S3 UF-SAR and FF-SAR, because neglectable differences were found for a SWH as high as 4.5 m in Section 3.1. In fact, a blurring of the S3 FF-SAR along-track IRF further reduces its differences with the UF-SAR IRF (shown for CS2 in Buchhaupt et al., 2021). The S6 FF-SAR waveforms and UF-SAR zero-Doppler beam waveforms did not compare so well, although this is expected over a stationary ocean surface, see Eq. 14. This is explained as follows: If the S6 FF-SAR along-track IRF $h_{FF}(x)$ is blurred to several tens of meters effective resolution instead, then ΔR_{rcmc} becomes significant over the footprint and the approximations leading

to Eq. 14 are no longer valid for FF-SAR, while UF-SAR is less affected. This provides another reason for the positive bias in Section 3.4, besides the non-vanishing grating lobes, when trying to fit S6 FF-SAR with the SAMOSA zero-Doppler beam. Since the SAMOSA model does not consider any surface motion effects, this issue requires a wave height correction for SAR altimetry in general (Egido et al., 2021a), and a separate correction for S6 FF-SAR. However, such a correction seems to either ask an unambiguous relationship between wave height and velocity variance as input, which can only be provided under strong assumptions on the ocean wave spectra (e.g. Elfouhaily et al., 1997) or requires input of a global wave spectral model. Any attempt to extract swell wave components directly from FF-SAR altimetry (Altiparmaki et al., 2022) would be an asset for such a correction.

5. Conclusion

We have demonstrated that S3 FF-SAR averaged ocean waveforms closely resemble the corresponding UF-SAR waveforms. We explain this with range-smearing of the grating lobes in the impulse response function (or point target response). This suggests that both S3 FF-SAR and UF-SAR waveforms can be retracked with the same waveform model, e.g. a physical SAMOSA model including all Doppler beams that would correspond to the FF-SAR coherent integration time, see Section 2.3. The same effects are present for CS2 FF-SAR, so the same arguments hold. No significant SSH and SWH biases between S3 UF-SAR and S3 FF-SAR are found when testing this approach over a single track segment.

S6 FF-SAR averaged ocean waveforms are much narrower than their UF-SAR counterparts. No exact correspondence with multilooked UF-SAR waveforms is found, but the S6 FF-SAR waveforms compare much better to the UF-SAR zero-Doppler beam. This correspondence has been explained by the suppression of the FF-SAR grating lobes, which makes the averaged waveform integrals similar in absence of sea surface motion. We have demonstrated how S6 UF-SAR waveform shapes can be emulated from S6 FF-SAR in this approximation, including the S6 grating lobes. This UF-SAR emulation strategy also leads to SWH estimates comparable to the EUMETSAT L2 product. It relies, though, on approximations which may increase the margin of error. Though the theoretically sound approach would be to develop an FF-SAR retracker for S6, our results suggest that the SAMOSA zero-Doppler beam can be a first workaround for S6 FF-SAR retracking in line with Egido and Smith (2017). No significant SSH bias between S6 UF-SAR and S6 FF-SAR are found when testing this approach over a single track segment, though a small SWH bias of 5 cm was present. This mismatch and the possible influence of sea surface motion on S6 waveforms needs to be assessed separately in future studies. Regarding future altimetry mission planning, it needs to be stressed that the CS2 and

S3 FF-SAR grating lobes can only be fully avoided by open-burst sampling as onboard the S6 satellite. If future missions aim to exploit the full potential of the FF-SAR technique for coastal altimetry, over sea ice, and for inland water targets, then the open-burst sampling mode is a crucial requirement.

Declaration of Competing Interest

Acknowledgments

Appendix A. Mission specific adjustments to the FF-SAR processor

This appendix outlines the details of our FF-SAR processor implementation, as far as it deviates from the implementation in Kleinherenbrink et al. (2020a), which is itself based on the work of Egido and Smith (2017). We also discuss mission-dependent adjustments for CS2, S3 and S6 altimeters.

Tracker range interpolation: The resulting L1b waveforms are all locally referenced to the same altitude over the reference ellipsoid, as long as this reference range does not deviate more than 1.15 m from the commanded instrument tracker range. Not only does this result in visually appealing and aligned radargrams as in Fig. 13, but it also fascilitates multilooking of consecutive FF-SAR waveforms without the need for prior range-alignment. If the waveforms were not aligned this way, multilooking would artificially widen and distort the waveforms' shapes, and hence introduce artificial biases to the retracked SSH and SWH.

RVP and RRP corrections: The RVP correction needs not to be applied to S6 pulse data, as the RVP is a residual phase of the deramp-on-receive radars CS2 and S3 only. Instead of using the same range history for all range bins, we follow the approach outlined by (Egido and Smith, 2017, Eq. 15). This can be regarded as a pure technicality, because asymmetric rotation-related range history differences dominate away from the equator in any case (Kleinherenbrink et al., 2020b).

Inter-burst phase jumps: FF-SAR altimetry processing was not foreseen at the time of CS2 and S3 mission design, and therefore, a phase alignment was strictly necessary within individual bursts only. We verify inter-burst phase jumps of $\pi/2$ for CS2 as in Kleinherenbrink et al. (2020a) and inter-burst phase jumps of π for both S3 satellites as in the ESA-reviewed FF-SAR code of Rieu et al. (2021a) over the Crete transponder. The instruments' manufacturer was not able to identify the cause of this issue (personal communication with T. Moreau, CLS). Those additional phase rotations are compensated for within our FF-SAR processing. For the most recent S6 mission, no such jumps are encountered.

Tracker range phase jumps: The satellite's tracker range (window delay) is constantly adjusted onboard to lock the range window to the Earth's surface, causing a phase jump coincident with each tracker range jump. The proportionality between tracker range change and phase rotation can be found directly for S6, corresponding to the additional residual range phase (RRP) caused by the tracker range adjustment. It is therefore given by the number of microwave wavelengths that fit into two meter (tracker range is only the one-way distance), namely

$$2\pi 2/\lambda = 2\pi 2 f_c/c \approx 569.0219 \text{ rad/m}, \tag{A.1}$$

which was also confirmed empirically over the Crete transponder. For S3 and CS2 this proportionality cannot be confirmed: The tracker range is adjusted for CS2 and S3 by steps of $c(2 \cdot 80e6)^{-1} \approx 1.8737$ m, with clock frequency $80e6$ Hz. Using the predicted proportionality from Eq. A.1 this would correspond to a residual phase rotation of

$$(-569.0219 \text{ rad/m} \times 1.8737 \text{ m}) \text{mod} 2\pi \equiv +0.625\pi. \tag{A.2}$$

However, we empirically determined a corresponding phase rotation of about $+0.82\pi$ over the Crete transponder instead, and Rieu et al. (2021a) independently defined a tracker_phase_shift of $+2.567 \approx +0.8171\pi$ [line 357 in l1b_processing.py], which is instead corrected for. This correction has been validated over multiple Crete transponder overpasses over time and appears to be shared among both S3 satellites. Furthermore, it varies not between the sites of the Svalbard and the Crete transponder for S3B for a limited number of overpasses, indicating no dependence on orbital parameters. In lack of other evidence, we therefore set the value $+0.82\pi$ as a constant in our processor. However, the exact value may be object to changes and further analysis over different types of targets needs to be done in order to understand the nature of this offset and to verify whether this assumption is valid.

Final phase calibration: Kleinherenbrink et al. (2020a) noticed a remaining parabola in the phase history after application of all phase corrections, which might be linked to an offset of the window-delay. Also Guccione et al. (2018) reported a remaining phase misalignment at this step, without providing more details. Also, at off-nadir positions and with increasing latitude, there will always be a remaining parabola in the phase history due to Earth's rotation (Kleinherenbrink et al., 2020b), which cannot be

compensated for due to the collection of signals from both cross-track directions at the same time. One way to compensate for the part of this parabola in nadir-looking direction is to introduce a small offset to the fast time in the RCMC (Kleinherenbrink et al., 2020a). To flatten the residual phase over transponder overpasses, we apply a fast time offset within the RCMC of 0.7 μs for CS2, 0.105 μs for S3 and −0.077 μs for S6.

Range bin masking: We approximately aligned the stack masks (range bin masks) to the CS2, S3, and S6 L1b products. This mask results from purely geometrical considerations for CS2 and S3 (due to the RCMC range bin shift). However, S6 has a reduced (varying) pulse repetition frequency of about 9 kHz, compared to approximately 18 kHz for CS2 and S3, in order to operate in a continuous, open-burst interleaved mode. As a consequence, the Doppler spectrum is undersampled, leading to spectral folding effects (see Section 7.3.13.4.2 Ambiguity mask in EUMETSAT (2022) or Fig. 7 in Donlon et al. (2021) for an example). The parts of the stack that are expected to contain significant aliased power are additionally masked in the stack before multilooking. The underlying assumption for this mask is that the waveform power before the leading edge is neglectable. We empirically find a good agreement when choosing range bin 47 (1-based indexing), or 93 (1-based indexing) with zero-padding factor of two, as the assumed leading edge onset.

Appendix B. Processor validation against ESA Level-1b products

For a validation of our processors we define two open ocean test cases, S3A-I and S6A-I (see Table 2), on which we compare the UF-SAR waveforms against the ESAs L1b product. All processing settings have been aligned with the ESA processor, including 180 bursts into S3A stacks and 473 bursts into S6A stacks, which correspond to approximately 2.292 s and 3.413 s target illumination time (integration time), respectively. No windowing is applied and the 'range walk' effect was simulated in our UF-SAR processing. The resulting waveforms have been range aligned to a common reference prior to obtaining Fig. B.16. We find that our UF-SAR implementation reproduces the EUMETSAT L1b power waveforms up to the speckle noise, but show here only the normalized averaged waveforms and their differences.

Overall, the agreement is excellent: Absolute differences of consistently less than 0.5% of the peak height are obtained for both cases, excluding the very trailing edge from range bin 90 onwards for S3. There, the difference likely originates from disagreements in the stack mask. Over the leading edge, the relative differences are as small as 3%. It needs to be stressed that the relative differences are only of importance where the power is not too small, because otherwise a tiny offset may cause misleadingly high percentage values.

Appendix C. Range de-focusing due to RCMC differences

In the following we want to formulate a model for the range-smearing as observed in the IRF over the transponder. We show in the following that this range-smearing is caused by a discrepancy between the applied RCMC for a nadir target and the range history of an along-track off-nadir target. In FF-SAR we apply a single RCMC to all range bins (all cross-track distances), because the differences of the range histories between a target at nadir and at any cross-track position is negligible with respect to the range resolution, as shown in Egido and Smith (2017). Therefore, we can limit the following discussion to an along-track target displacement only. For simplicity, we approximate that the satellite passes with constant velocity V and constant heigth rate $\dot{H}$ over a flat Earth. The applied RCMC at a time η consists of two terms, namely

$$R_{rcmc}(t;\eta) = R(t;\eta) - H(\eta) - f_c v_r(t;\eta)/s. \quad (C.1)$$

Here, t denotes the pulse time delay $t \in [-T/2, T/2]$ with respect to the nadir looking satellite position at time η. The first term describes the range history of the satellite to a surface point that is in nadir direction at time η and H is the altitude of the satellite above the surface. The third term describes the additional, apparent range shift due to the Doppler effect. This RCMC is not accurate for a target that is in nadir at time $\eta - dt$, so we aim to evaluate the difference between the correct and the applied RCMC

$$\Delta R_{rcmc}(t;\eta, dt) = R_{rcmc}(t+dt;\eta-dt) - R_{rcmc}(t;\eta) \quad (C.2)$$
$$= \Delta R(t;\eta, dt) - f_c \Delta v_r(t;\eta, dt)/s. \quad (C.3)$$

where the reference range $H(\eta)$ cancels out. Here we similarly define the differences

$$\Delta R(t;\eta, dt) = R(t+dt;\eta-dt) - R(t;\eta) \quad (C.4)$$
$$\Delta v_r(t;\eta, dt) = v_r(t+dt;\eta-dt) - v_r(t;\eta). \quad (C.5)$$

We calculate now explicitly the range history $R(t,\eta)$

$$R(t;\eta) = \sqrt{[H(\eta) + Vt\sin\alpha]^2 + [Vt\cos\alpha]^2} \quad (C.6)$$

$$= H(\eta)\sqrt{1 + \frac{2Vt\sin\alpha}{H}(\eta) + \left(\frac{Vt}{H(\eta)}\right)^2} \quad (C.7)$$

with $\alpha = \arcsin(\dot{H}/V)$ and satellite height rate $\dot{H}$. Since $\sqrt{1+\epsilon} \approx 1 + \epsilon/2$ (for small ϵ) we can safely approximate

$$R(t;\eta) \approx H(\eta) + Vt\sin\alpha + \frac{(Vt)^2}{2H(\eta)}$$

$$= H(\eta) + t\dot{H} + \frac{V^2 t^2}{2H(\eta)} \quad (C.8)$$

which results in an error of about 2 mm for S6 with $T = 3.413$ s at high pitch angles. Additionally, the pitch angles are required for the evaluation of the radial velocity to the nadir target at time η. We use $x = Vt\cos\alpha \approx Vt$ for the ground projected distance and
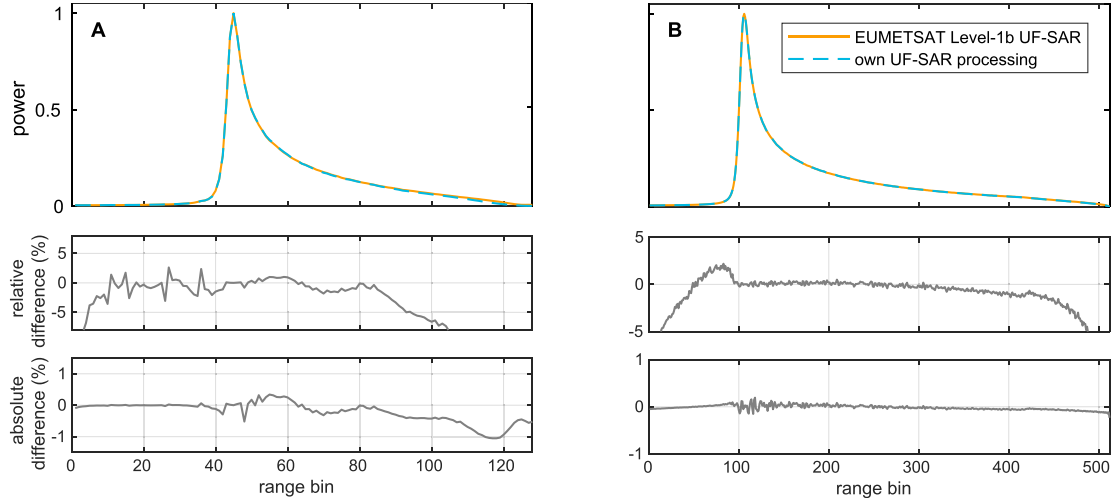
Fig. B.16. Comparison of our UF-SAR processing according to Egido et al. (2021b) against EUMETSAT's Level-1b products for case S3A-I in column A and S6A-I in column B. The relative difference of the normalized waveforms is defined as 100·(emulated - L1b)/L1b [%] and the absolute difference as 100·(emula.ted - L1b) [%].

$\theta = \arctan\left(x/\left(H(\eta) + \dot{H}t\right)\right) \approx Vt/H(\eta)$ for the pitch angle, where we used $\left(H(\eta) + \dot{H}t\right)^{-1} \approx 1/H(\eta)$. We can also safely approximate $\alpha \approx \sin\alpha = \dot{H}/V$ due to the small angle α. With these definitions, the radial velocity from the target to the satellite becomes

$$v_r/V = \sin(\theta + \alpha) \approx \theta + \alpha \approx Vt/H(\eta) - \dot{H}/V \qquad (C.9)$$

$$\iff v_r(t;\eta) \approx V^2 t/H(\eta) - \dot{H}. \qquad (C.10)$$

By plugging Eqs. C.8 and C.10 into Eqs. C.4 and C.5 and using the Taylor expansion $H(\eta - dt) = H(\eta) - \dot{H}dt$, it can be shown that

$$\Delta R(t;\eta,dt) \approx \frac{V^2}{H(\eta)}\frac{dt}{t}t + \frac{V^2 dt^2}{2H(\eta)} \quad \text{and} \qquad (C.11)$$

$$\Delta v_r(t;\eta,dt) \approx V^2 dt/H(\eta), \qquad (C.12)$$

which becomes

$$\Delta R(t;\eta,x) \approx \frac{Vx}{H(\eta)}t + \frac{x^2}{2H(\eta)} \quad \text{and} \qquad (C.13)$$

$$\Delta v_r(t;\eta,x) \approx \frac{Vx}{H(\eta)} \qquad (C.14)$$

when being rewritten in terms of the ground projected along track distance x of the point scatterer via $dt = x/(V\cos\alpha) \approx x/V$. Therefore, the RCMC difference in Eq. C.3 is a linear function of t

$$\Delta R_{rcmc}(t;\eta,x) \approx \frac{Vx}{H(\eta)}t + \frac{x^2}{2H(\eta)} - \frac{xf_c V}{H(\eta)s}$$

$$= \dot{R}(\eta)t + R_0(\eta) \qquad (C.15)$$

comprising three components: i) $VxtH^{-1}$ describes the range widening of the IRF between the outermost pulses, e.g. when plugging in -T/2 and T/2. ii) $x^2(2H)^{-1}$ describes the total range offset of the point target within the range win-

dow due to its along track distance x. iii) $f_c Vx(Hs)^{-1}$ describes a range offset caused by the differences of applied and correct Doppler shift correction.

Appendix D. Doppler rate

In order to compute the Doppler rate $|FM| = \dot{f}_D = 2f_c\dot{v}_r/c$, we need to compute the fast-time derivative $\partial/\partial t$ of the radial velocity between target and satellite v_r. Using the result from Eq. C.10, we obtain

$$\dot{v}_r(\eta) \approx \frac{V^2}{H(\eta)}. \qquad (D.1)$$

Since the changes in the factor $1/H(\eta)$ over the time T are negligible (several meters vs several hundred kilometers), we obtain

$$|FM| = \dot{f}_D \approx \frac{2f_c V^2}{cH}. \qquad (D.2)$$

References

Abdalla, S., Dinardo, S., Benveniste, J. et al., 2018. Assessment of CryoSat-2 SAR mode wind and wave data. Adv. Space Res. 62(6), 1421–1433. URL: https://www.sciencedirect.com/science/article/pii/S0273117718301121. https://doi.org/10.1016/j.asr.2018.01.044.

Alpers, W., Rufenach, C., 1979. The effect of orbital motions on synthetic aperture radar imagery of ocean waves. IEEE Trans. Antenn. Propagat. 27 (5), 685–690. https://doi.org/10.1109/TAP.1979.1142163, Conference Name: IEEE Transactions on Antennas and Propagation.

Altiparmaki, O., Kleinherenbrink, M., Naeije, M., et al., 2022. SAR altimetry data as a new source for swell monitoring. Geophys. Res. Lett. 49 (7). https://doi.org/10.1029/2021GL096224, e2021GL096224, URL: https://onlinelibrary.wiley.com/doi/abs/10.1029/2021GL096224. _eprint: https://onlinelibrary.wiley.com/doi/pdf/10.1029/2021GL096224.

Amarouche, L., Tran, N., Herrera, D., et al., 2019. Impact of the ocean waves motion on the delay/doppler altimeters measurements. In: 019 Ocean Surface Topography Science Team (OSTST) Meeting.

Amraoui, S., Moreau, T., Vayre, M., et al., 2022. Ffsar replica removal algorithm for closed-burst data. In: 2022 Living Planet Symposium.

Aublanc, J., Dinardo, S., Cadier, E., et al., 2020. Impact of the range walk processing in the sentinel-3a sea level trend. In: 2022 Ocean Surface Topography Science Team (OSTST) meeting.

Aublanc, J., Moreau, T., Amraoui, S., et al., 2022. Assessment of the sentinel-3 fully focused SAR processing over the Antarctic ice sheet. In: 2022 Living Planet Symposium.

Boisot, O., Amarouche, L., Lalaurie, J.-C. et al., 2016. Dynamical properties of sea surface microwave backscatter at low-incidence: correlation time and doppler shift. IEEE Trans. Geosci. Remote Sens. 54(12), 7385–7395. https://doi.org/10.1109/TGRS.2016.2601242. Conference Name: IEEE Transactions on Geoscience and Remote Sensing.

Brown, G., 1977. The average impulse response of a rough surface and its applications. IEEE Trans. Antenn. Propagat. 25 (1), 67–74. https://doi.org/10.1109/TAP.1977.1141536, Conference Name: IEEE Transactions on Antennas and Propagation.

Buchhaupt, C., 2019. Model Improvement for SAR Altimetry Ph.D. thesis. Technische Universität Darmstadt.

Buchhaupt, C., Fenoglio, L., Becker, M., et al., 2021. Impact of vertical water particle motions on focused SAR altimetry. Adv. Space Res. 68 (2), 853–874. https://doi.org/10.1016/j.asr.2020.07.015, URL: https://linkinghub.elsevier.com/retrieve/pii/S0273117720304920.

Buchhaupt, C., Fenoglio-Marc, L., Dinardo, S., et al., 2018. A fast convolution based waveform model for conventional and unfocused SAR altimetry. Adv. Space Res. 62 (6), 1445–1463. https://doi.org/10.1016/j.asr.2017.11.039, URL: https://www.sciencedirect.com/science/article/pii/S0273117717308505.

Dinardo, S., 2020. Techniques and Applications for Satellite SAR Altimetry over water, land and ice. Ph.D. Thesis Technische Universität Darmstadt. URL: https://tuprints.ulb.tu-darmstadt.de/11343/ iSBN: 9783935631457 Volume: 56.

Donlon, C.J., Cullen, R., Giulicchi, L. et al., 2021. The Copernicus Sentinel-6 mission: Enhanced continuity of satellite sea level measurements from space. Remote Sens. Environ. 258, 112395. URL: https://www.sciencedirect.com/science/article/pii/S0034425721001139. doi:10.1016/j.rse.2021.112395.

Egido, A., Buchhaupt, C., Boy, F. et al., 2021a. Correcting for the discrepancies in the hr swh measurements. In: 2021 Sentinel-6 Validation Team Meeting.

Egido, A., Dinardo, S., Ray, C., 2021b. The case for increasing the posting rate in delay/Doppler altimeters. Adv. Space Res. 68 (2), 930–936. https://doi.org/10.1016/j.asr.2020.03.014, URL: https://linkinghub.elsevier.com/retrieve/pii/S0273117720301691.

Egido, A., Ray, C., 2019. On the Effect of Surface Motion in SAR Altimeter Observations of the Open Ocean. In: 2019 Ocean Surface Topography Science Team (OSTST) Meeting.

Egido, A., Smith, W.H.F., 2017. Fully focused SAR altimetry: theory and applications. IEEE Trans. Geosci. Remote Sens. 55 (1), 392–406. https://doi.org/10.1109/TGRS.2016.2607122, Conference Name: IEEE Transactions on Geoscience and Remote Sensing.

Elfouhaily, T., Chapron, B., Katsaros, K., et al., 1997. A unified directional spectrum for long and short wind-driven waves. J. Geophys. Res.: Oceans 102 (C7), 15781–15796. https://doi.org/10.1029/97JC00467, URL: https://onlinelibrary.wiley.com/doi/abs/10.1029/97JC00467. _eprint: https://onlinelibrary.wiley.com/doi/pdf/10.1029/97JC00467.

EUMETSAT, 2022. Sentinel-6/Jason-CS ALT Level 1 Product Generation Specification (L1 ALT PGS) — EUMETSAT. URL: https://www.eumetsat.int/media/48261.

Guccione, P., 2008. Beam sharpening of delay/doppler altimeter data through chirp zeta transform. IEEE Trans. Geoscie. Remote Sens. 46 (9), 2517–2526. https://doi.org/10.1109/TGRS.2008.918863. Conference Name: IEEE Transactions on Geoscience and Remote Sensing.

Guccione, P., Scagliola, M., Giudici, D., 2018. 2D frequency domain fully focused SAR processing for high PRF radar altimeters. Remote Sens. 10(12), 1943. URL: https://www.mdpi.com/2072-4292/10/12/1943. https://doi.org/10.3390/rs10121943. Number: 12 Publisher: Multidisciplinary Digital Publishing Institute.

Jugier, R., Ablain, M., Fraudeau, R. et al., 2022. On the uncertainty associated with detecting global and local mean sea level drifts on Sentinel-3A and Sentinel-3B altimetry missions. Ocean Sci. 18(5), 1263–1274. URL: https://os.copernicus.org/articles/18/1263/2022/. https://doi.org/10.5194/os-18-1263-2022. Publisher: Copernicus GmbH.

Kleinherenbrink, M., Naeije, M., Slobbe, C. et al., 2020a. The performance of CryoSat-2 fully-focussed SAR for inland water-level estimation. Remote Sens. Environ. 237, 111589. URL: https://linkinghub.elsevier.com/retrieve/pii/S0034425719306091. https://doi.org/10.1016/j.rse.2019.111589.

Kleinherenbrink, M., Smith, W.H., Naeije, M.C. et al., 2020b. The second-order effect of Earth's rotation on Cryosat-2 fully focused SAR processing. J. Geodesy, 94(1). URL: http://www.scopus.com/inward/record.url?scp=85077329577&partnerID=8YFLogxK. https://doi.org/10.1007/s00190-019-01337-8.

McMillan, M., Egido, A., Muir, A.S., 2020. First Assessment of Fully Focused SAR Altimetry over Ice Sheets, 2020, C034–07W. URL: https://ui.adsabs.harvard.edu/abs/2020AGUFMC034...07M. Conference Name: AGU Fall Meeting Abstracts ADS Bibcode: 2020AGUFMC034...07M.

Moreau, T., Amraoui, S., Cadier, E., et al., 2022. Exploitation of fully focussed SAR (FFSAR) processing using s6-mf over ocean. In: 2022 Living Planet Symposium.

Moreau, T., Rieu, P., Aublanc, J. et al., 2017a. Investigation of SWH bias in SAR altimetry mode. In: 2017 Ocean Surface Topography Science Team (OSTST) Meeting.

Moreau, T., Rieu, P., Aublanc, L. et al., 2017b. Investigation of swh bias in sar altimetry mode. In: 2017 Ocean Surface Topography Science Team (OSTST) Meeting.

Moreau, T., Tran, N., Aublanc, J. et al., 2018. Impact of long ocean waves on wave height retrieval from SAR altimetry data. Adv. Space Res. 62 (6), 1434–1444. URL: https://linkinghub.elsevier.com/retrieve/pii/S0273117718304708. https://doi.org/10.1016/j.asr.2018.06.004.

Nielsen, K., Altiparmaki, O., Fenoglio-Marc, L. et al., 2021. A New Fully-Focused SAR Altimetry Processor in the ESA G-POD SARvatore Family: Validation and Applications on Inland Waters. https://doi.org/10.13140/RG.2.2.28915.40485.

Passaro, M., Rose, S.K., Andersen, O.B. et al., 2018. ALES+: Adapting a homogenous ocean retracker for satellite altimetry to sea ice leads, coastal and inland waters. Remote Sens. Environ. 211, 456–471. URL: https://www.sciencedirect.com/science/article/pii/S0034425718300920. https://doi.org/10.1016/j.rse.2018.02.074.

Quartly, G.D., Nencioli, F., Raynal, M. et al., 2020. The Roles of the S3MPC: Monitoring, Validation and Evolution of Sentinel-3 Altimetry Observations. Remote Sens. 12(11), 1763. URL: https://www.mdpi.com/2072-4292/12/11/1763. https://doi.org/10.3390/rs12111763. Number: 11 Publisher: Multidisciplinary Digital Publishing Institute.

Raney, R., 1998. The delay/Doppler radar altimeter. IEEE Trans. Geosci. Remote Sens. 36(5), 1578–1588. https://doi.org/10.1109/36.718861. Conference Name: IEEE Transactions on Geoscience and Remote Sensing.

Ray, C., Martin-Puig, C., Clarizia, M., et al., 2015. SAR altimeter backscattered waveform model. IEEE Trans. Geosci. Remote Sens. 53, 911–919. https://doi.org/10.1109/TGRS.2014.2330423.

Raynal, M., Moreau, T., Tran, N., et al., 2018. Assessment of the sarm processing sensitivity to swell. In: 2018 Ocean Surface Topography Science Team (OSTST) meeting.

Rieu, P., Amraoui, S., Restano, M., 2021a. SMAP (Standalone Multi-mission Altimetry Processor). https://doi.org/10.5270/esa-cnes-sentinel-3.smap.

Rieu, P., Moreau, T., Amarouche, L., et al., 2018. From unfocused to fully focused SAR processing: illustrations of potential benefits for

different surfaces. In: 2022 Ocean Surface Topography Science Team (OSTST) meeting.

Rieu, P., Moreau, T., Cadier, E. et al., 2021b. Exploiting the Sentinel-3 tandem phase dataset and azimuth oversampling to better characterize the sensitivity of SAR altimeter sea surface height to long ocean waves. Adv. Space Res. 67(1), 253–265. URL: https://linkinghub.elsevier.com/retrieve/pii/S0273117720306840. https://doi.org/10.1016/j.asr.2020.09.037.

Scagliola, M., Dinardo, S., Fornari, M., 2015. An extended analysis of along-track antenna pattern compensation for SAR altimetry. In: 2015 IEEE International Geoscience and Remote Sensing Symposium (IGARSS), pp. 1238–1241. https://doi.org/10.1109/IGARSS.2015.7325997, iSSN: 2153-7003.

Scagliola, M., Recchia, L., Maestri, L. et al., 2021. Evaluating the impact of range walk compensation in delay/Doppler processing over open ocean. Adv. Space Res. 68(2), 937–946. URL: https://www.sciencedirect.com/science/article/pii/S0273117719308403. https://doi.org/10.1016/j.asr.2019.11.032.

Schlembach, F., Passaro, M., Dettmering, D. et al., 2022. Interference-sensitive coastal SAR altimetry retracking strategy for measuring significant wave height. Remote Sens. Environ. 274, 112968. URL: https://www.sciencedirect.com/science/article/pii/S0034425722000827. https://doi.org/10.1016/j.rse.2022.112968.

Vignudelli, S., Kostianoy, A.G., Cipollini, P. et al., (Eds.), 2011. Coastal Altimetry. Berlin, Heidelberg: Springer, Berlin Heidelberg. URL: http://link.springer.com/10.1007/978-3-642-12796-0. https://doi.org/10.1007/978-3-642-12796-0.